ORDERED-PHASES OF ASYMMETRIC AB-BLOCK COPOLYMER MELTS CONFINED INTO CIRCULAR ANNULAR DISCS: A COMPUTATIONAL STUDY

MUHAMMAD JAVED IQBAL *

Department of Mathematics, Shah Abdul Latif University Khairpur.
*Corresponding Author Email: mjaved.iqbal@salu.edu.pk,
ORCID ID: https://orcid.org/0009-0000-1737-1826

INAYATULLAH SOOMRO

Department of Mathematics, Shah Abdul Latif University Khairpur.
Email: inayat.soomro@salu.edu.pk, ORCID ID: https://orcid.org/0000-0001-6423-1009

USAMA GULZAR

Department of Mathematics, Shah Abdul Latif University Khairpur.
Email: usama.gulzar@salu.edu.pk, ORCID ID: https://orcid.org/0009-0007-1353-1272

MUHAMMAD SALMAN JAVED

Department of Mathematics, Shah Abdul Latif University Khairpur.
Email: salman.javed@salu.edu.pk, ORCID ID: https://orcid.org/0009-0003-9207-951X

Abstract

Over the past decade, nanotechnology has set the industrial world on a new development path. Experimental and theoretical scientists are interested in discovering new structures of soft materials with potential applications in nanotechnology, including nanoporous storage media, fabrication for nanoelectronics, soft robotics, energy harvesting, and biomedical. Mathematicians are predicting novel morphologies of diblock copolymer systems through mathematical modelling and computer simulations studying nanostructures in the presence of a surface field, which leads to the identification of new dimensions of melt. Confinement improves the frustration in nanostructures and leads to new patterns of nanoparticles. The computational study of novel nanostructures is done through simulation models. The cell dynamic simulation model provides large-scale simulations of nanomaterials quickly and efficiently. This computational investigation confines lamellar, cylindrical, and spherical structures into asymmetric diblock copolymers ($f_A \neq f_B$) in circular annular discs. For the simulations requirement of this model, the continuum macromolecule of the diblock copolymers system is discretized on a 17-point isotropic stencil to approximate the Laplacian in a polar mesh. FORTRAN codes have been developed for the PDEs included in the model. The simulation results are visualized with Open Dx.

Keywords: Numerical Solutions of PDEs, Finite Difference Method, Polar Mesh System, Discretization, Soft Materials, Nanotechnology, Diblock Copolymers, Cell Dynamics Simulation, Confinement.

1. INTRODUCTION

In this computational study, a template to solve the PDE entanglement in CDS models through the finite difference method (FDM) in polar geometries is developed. This aims to detect the changes occurring in the system due to self-assembly and phase separation under confinement. This study explores how the curvature of circular annular pores and the confinement affect the self-organization in diblock copolymers. The study has been demonstrated through computational simulations with the CDS model in polar geometry

and existing experimental validation. The cell dynamic Simulations predicted lamellar structures and concentric rings to grow spontaneously inside pores. The observed morphologies based on the curvature effect closely matched experimental results. The change of curvature, volume fraction of each block in the system, and confinement are key tuning parameters used to predict the order phases of the asymmetric diblock copolymer system. The study of materials at the scale of 1 to 100 nanometres is called nanoscience (developed by famous physicist Feynman, 1959), based on which nanomaterials are produced. This theory was introduced during his lecture, in which he proposed building smaller but more efficient machines in real-life systems. Nanoscience is a newly emerging field encompassing many scientific disciplines, such as physics, chemistry, materials science, biomedical science, computer science, and mathematics. Nanomaterials that are very small in size have unique surface-to-volume ratios and properties. Taniguchi (1974) coined "nanotechnology" to fabricate soft materials. Nanotechnology is the name of manipulating and engineering materials at the nanoscale, in which miniaturization ideas are applied. The unique properties of nanomaterials differ from their bulk form. These properties provide various applications, including material energy harvesting, biotechnology, drug delivery, intelligence, and environmental remediation. [1-4]. Soft materials are condensed matter physical materials that are neither fully solid nor fully liquid but have properties between these two states. Polymers are one of the basic types of soft materials, while other types include surfactants, colloids, and liquid crystals [5]. The study focuses on many constraints, including confinement, pressure, electric, and magnetic fields. The study of soft matter utilizes different research methods. These methods use computer simulations and theoretical models to study self-assembly, phase separation, rheology, and biological materials [6-7]. Two strategies play a crucial role in creating nanodevices: top-down and bottom-up. This manufacturing strategy brings numerous benefits, including high throughput, outstanding performance, accuracy, stability, scalability, and compatibility, significantly reducing costs. Nanolithography, sensors, nanophotonic, nano solar cells, ultrafiltration nanomembranes, non-volatile memory, and bit-patterned media are all application examples [8-17]. A linear AB-diblock copolymer system is constructed by covalently grafting two homopolymer blocks that are thermodynamically incompatible within the same macromolecule, as Shown in Figure 1.
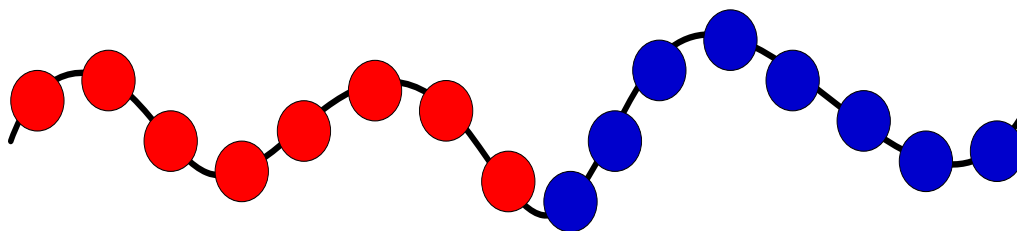

Figure 1: AB-Diblock Copolymers

Self-assembly and phase separation in the diblock polymer system, driven by the repulsion between blocks, create different nanostructure patterns. Factors influencing the prediction of these new nanostructures include block size, architecture, interactions, and

surface field geometry. Experimental and theoretical study of the diblock copolymers system reveals that the bulk-phase diagram, shown in Figure 2, contains some ordered microphase domains, including parallel lamellae, hexagonal packing of cylinders, body-centered matrices of spheres, and bicontinuous complex gyroids.
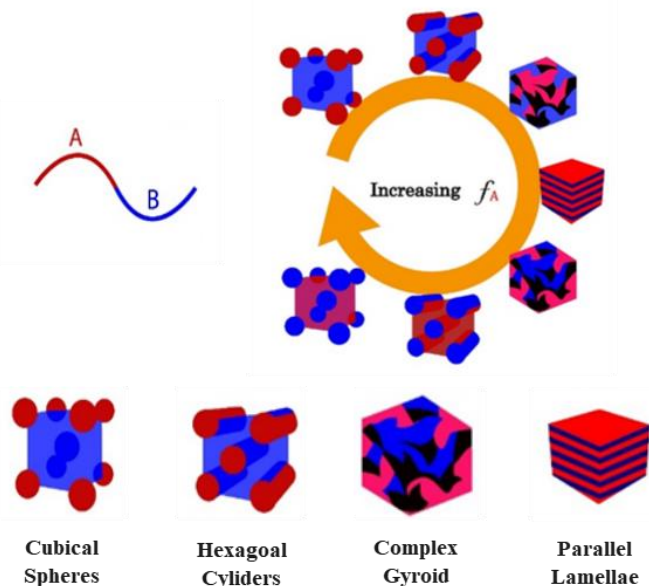

Figure 2: Phase diagram of diblock copolymers system

A balance between the χN and the entropy of mixing tunes the morphology formation in diblock copolymer systems. A higher molecular weight in this regard provides better control in favor of separation. Each copolymer junction point between different blocks introduces an energetic penalty quantified by χN, where χ is the Flory-Huggins interaction parameter and N is the degree of polymerization. Tuning up the value of N increases χN which promotes microphase separation. Higher molecular weight chains confer additional conformational degrees of freedom at the boundaries between domains. This loss of chain entropy leads to higher interfacial tension, which is a significant propulsion for microphase separation. Higher molecular weight polymers require more thermal energy (higher temperature or longer time) during self-assembly to fully expand and relax into the equilibrium structure.

It confines the system into discrete periodic domains through kinetic trapping. Domain spacing and other structural characteristics can be influenced by molecular weight. Block copolymer nanostructures can be customized for biomaterial templates and nanolithography by tuning N [18-22]. The diblock copolymer develops a body-centered cubic, spherical crystal structure when the volume fraction of one block is low. In this construction, the other block surrounds the spherical domains of one block that are set up in a periodic lattice. The structure changes to hexagonally packed cylinders of one block embedded in a matrix of the other block as the volume ratio gets closer to each other.Perforated lamellar structures, in which the parallel layers are intermittently

disrupted by faults or pores filled with the minority block. The Flory-Huggins interaction (χ), the degree of polymerization (N), and the temperature (T) are parameters used in the computational modelling of diblock copolymer systems to build desired structures and attributes. The Flory-Higgins interaction parameter (χ) measures the thermodynamic interaction between two blocks of a diblock copolymer. High levels of encouraging the establishment of orderly phases and a predictor for phase separation are also indicated. Blocks tivide into higher-value systems, producing phases with distinct borders like lamellar, cylindrical, or spherical forms. The degree of polymerization (N) is the number of repetition units in each copolymer block. By altering the overall size and structure of the copolymer chains, N affects the formation and stability of various phases. Longer polymer chains (N increases) can affect phase behaviour and lead to specific phase transitions or morphologies. The ordered phases and stability in diblock copolymer systems are influenced by temperature (T).

Phase transitions brought on by temperature variations can alter the ordered structures that form (for instance, lamellar to gyroid transitions). Thermal energy can alter or enhance interactions between polymer blocks to change the phase morphology and transition between ordered phases. Greater T encourages the disordered mixed state through increased entropy and improved chain mobility. Decreasing temperature T also decreases chain flexibility, increasing macrophase phase separation. To improve this microphase separation, the degree of segregation χN is increased by tuning up χ or N. In this context, the quantity N measures the equilibrium between the repulsion forces and the entropy brought on by chain conformation. An order-disorder transition occurs when $\chi N \sim 10.5 - 15$, which creates distinct periodic structures. The system underwent a dramatic transition and entered a condition characterized by robust segregation above a higher threshold, $\chi N \sim 30 - 40$. The system transforms from disordered spheres/cylinders to ordered structures like lamellae or gyroids that reduce the interfacial area by increasing χN through χ, N or decreasing T [23-26].

1.1 Confinement in Diblock Copolymers

Confinement in diblock copolymers is a powerful method for preparing nanostructures with precise shapes. This surface field offers various applications in nanotechnology, including creating templates, nanoporous materials, artificial muscles, and other responsive materials [27]. Confinement affects how the diblock copolymer self-assembles. Diblock copolymers can be used for this by encapsulation in a thin film, porous template, or other confined area. The confined boundary can significantly affect the morphology of self-assembled nanostructures. In diblock copolymers, confinement affects the temperature at which the order-disorder transition occurs. Block copolymers that typically exhibit a second-order order-disorder transition in the absence of confinement may instead show a first-order order-disorder transition when subjected to confinement [28]. Several nanotechnology applications are possible for entrapment in diblock copolymers. For example, containing diblock copolymers can create templates for producing nanowires and nanotubes. In addition, they can be used to produce nanoporous materials with regulated pore size and morphology. Confined diblock

copolymers can also produce synthetically responsive materials [29]. Diblock copolymers are confined in attractive walls to investigate the effects of different compartment sizes and geometries on self-assembly. In soft confinement systems, conformal walls study tunable confinement forces without completely restricting movement like rigid walls, which provide adjustable repulsive stresses to the chains [30-32]. Cell dynamics models add confinement to one or two-dimensional periodic boundary conditions that resemble thin films or cylinders. As a result, morphologies are constrained, and interfaces are introduced, competing with microphase separation. Different patterns, such as multilayers perpendicular to surfaces or parallel cylinders, are created. The degree of confinement is controlled by varying the film thickness or cylinder diameter about the bulk spacing. Strong confinement produces pattern faults and disturbs periodic order [33]. Feng and Ruckenstein utilized self-consistent field theory to simulate diblock copolymers inside cylindrical pores with various diameters. Contrary to bulk, cylindrical confinement limits the development of morphology to structures with a thin interface parallel to the pore walls, suppressing typical bulk phases below a specific diameter. As a result of the conflict between bulk segregation and interface effects, distinctive restricted structures like rings and helices are created.

There are clear phase transitions that are diameter-sensitive. Near interfaces, confinement results in increased chain stretching costs, symmetry breakdowns, and form distortions. Constrictions controlled by surface segregation preferences can kinetically sustain non-equilibrium morphologies and enhance order-disorder transitions. Insight into composition, nanostructure, and confinement relationships at the molecular level is provided via simulations [34]. When diblock polymers are confined, the frustration between the blocks in the small space leads to the disruption of equilibrium and the formation of newly ordered phases. With drug delivery and separation media applications, confinement within pores changes structural frustration through pore size to generate unique morphologies. As a result of a mixture of entropy, frustration, and interface effects that disrupt symmetry, melts in confinement display more complicated shapes [35-36]. A deeper understanding of how confinement affects block copolymer behaviour is provided by introducing simulation methods such as self-consistent field (SCF) theory and coarse-graining. Xiang et al. have described the effects of confinement on block copolymers and their implications for material patterning and design. [37].

A detailed examination of the universal and copolymer-specific parameters affecting confinement-based morphological control is provided by Yang et al. Using simulations, they look into the morphologies of cylindrical diblock contained in cylindrical pores. It identifies the components of composition, pore size, and system-specific factors affecting constrained self-assembly. Parallel cylinders along pores form above a threshold; complicated structures like helices form below it. Similar to bulk phases, confinement causes distinct topological modifications. It is demonstrated that there is only sometimes a connection between composition, fraction, and architecture under confinement. Composition, architecture, and defect generation regulate chain stretching and interface energies to balance bulk and surface segregation. Restrictive nanostructures' experimental observations are interpreted and forecasted using insights [38].

Confinement of soft materials in polar, cylindrical, or spherical geometries affects the material's physical properties by changing the arrangement of the soft material chains. The orientation of the domains results in the rearrangement of defects that differentiate the material from other materials due to changes in stiffness, flexibility, and other properties [39]. Soomro et al. use mathematical models to provide molecular insight into self-assembly under multi-axial geometric constraints. In contrast to simple cylinders, concentric inner/outer surfaces are introduced in SCF simulations of cylinder-forming diblock copolymers within annular pores. Calculations provide asymmetric nested or concentric cylinder topologies that are stable under confinement by considering block repulsion, stretching, and surface interactions using a free energy functional. In contrast to annular thickness/bulk spacing, phase space maps suggest preferred topologies based on confinement, composition, and surface affinities.

Compared to atomistic approaches, simulation captures morphologies that are empirically challenging across a wider parameter range. The use of numerous confinement geometries to self-assemble complicated structures is made clear by insights [40].

Transforming a physical problem into a boundary-fitted curvilinear coordinate system can often simplify the analysis by eliminating the need to deal with irregular or arbitrarily shaped boundaries. In such a coordinate system, the coordinate lines follow the boundary's shape, making it easier to impose boundary conditions and solve the governing equations. In polar coordinates, the coordinate lines are circular, which is well-suited for problems with circular symmetry [41-44].

Iqbal et al. focused on curved geometries and predicted new patterns and defects in lamellae forming system [45], cylindrical forming system [46], and spherical forming system [47] by discretization of a macromolecule of diblock copolymers with 9-point stencils constructed by finite difference numerical scheme in polar geometry.

The lamellae formulation is also presented by modification of the discretizational scheme into a diagonal discretization scheme [48]. Cell dynamic simulation's algorithm and flow chart are modified, coded, and executed for curved geometries and confinement [49].

2. MATERIALS AND METHODS

Grid-point methods are numerical techniques used to solve partial differential equations (PDEs) by discretizing the domain of the problem into a grid. Due to its 2nd-order partial differential equation nature, the Laplace equation is challenging to solve analytically for complicated geometries. FDM reduces the PDE to a set of algebraic equations that may be solved on a grid by approximating the derivatives as finite difference quotients. Different expressions for the derivatives are developed to choose an accurate approximation, and their truncation errors are examined [50-56]. A Cartesian coordinate system is unsuitable for this purpose since it is uniform and orthogonal everywhere. Therefore, curvilinear coordinates, shown in Figure 3, generate grids with non-uniform spacing, allowing grid points to be clustered or spread out as needed. In confinement, the polar coordinate representation is particularly suited to analyzing block copolymer

systems that exhibit preferential radial ordering. Both theory and interpretation are made simpler by it. A discretized grid approximates the polar coordinate system's partial differential equations (PDEs) using the Finite Difference Method (FDM) discretization in the polar mesh. This technique enables us to solve PDEs and estimate derivatives numerically by dividing the polar domain into discrete points
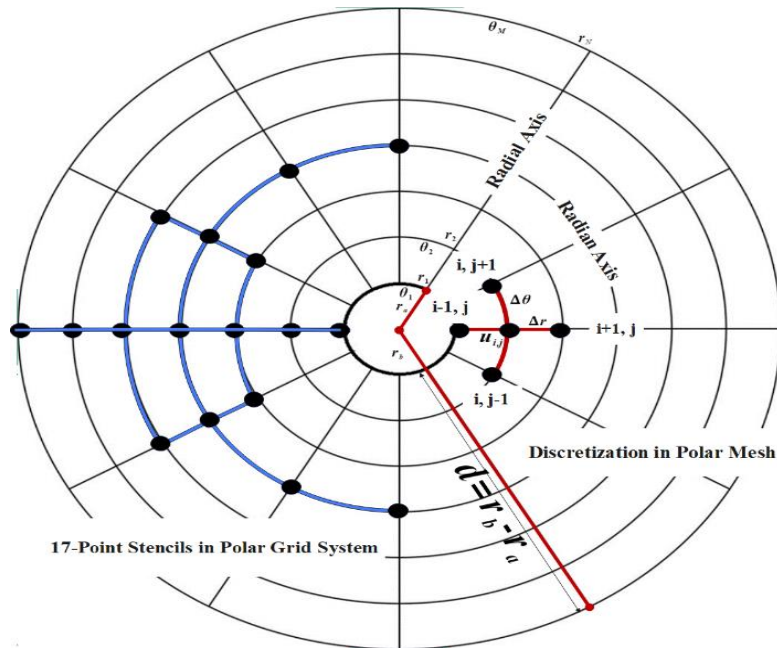

Figure 3: Discretization in polar mesh

In the left half of Figure 3, a 17-point stencil is presented on the polar grid, while the discretization procedure in the polar mesh system is in the right half of the figure. The point $u_{i,j}$ is an average point of the nearest four points approximated for Laplacian in polar mesh along the radial and radian axis. We Discretize the domain into a polar grid of discs with discrete radial points $r_1, r_2, ... r_N$ and angular points $\theta_1, \theta_2, ... \theta_M$. The computational domain and boundary conditions are defined. The internal radius is r_a is fixed to avoid singularity issues. The external radius of the polar disc is r_b to get various pore sizes d of the polar disc. The radial domain is graduated into Δr step size for periodic boundary conditions and the radian domain is graduated in $\Delta \theta$ step size for reflected boundary conditions.

2.1 Simulations Model

The choice of simulation method depends on the specific questions being addressed and the computational resources available. Different methods have different strengths and weaknesses. TDGL is a coarse-grained, continuum-based method approximating free energy with time-dependent Ginzburg-Landau functionality. Molecular Dynamics models (MD) and Monte Carlo models (MC) are more atomistic approaches that explicitly simulate the motion of individual molecules or particles. Dissipative Particle Dynamics (DPD) models and Bond Fluctuation (BD) models are mesoscale models that observe the

motion of a group of particles instead of an individual particle. Self-consistent field theory (SCFT) is a mean-field model that observes the free energy of a system during the transition of particles in soft materials. This model is computationally efficient and consistent with the equilibrium properties of the diblock copolymers system. Its time-dependent extension is DSCFT, which is used to observe the flow effect [57-64]. Due to its computational efficiency and reduced cost, the CDS model is used to observe the self-assembly and phase transition in the diblock copolymers for larger time steps. CDS model is a coarse-grained method that neglects some of the molecular-level details of the system; however, the accuracy of CDS can be improved by incorporating more detailed information about the system, such as the interactions between different types of polymer segments [65]. The model is simplified by lattice representation while retaining the basic physics of microphase separation in copolymers. This enables efficient simulation of quite empirically relevant systems. Variables involved in Lattice can represent A-rich or B-rich cells by taking values of 1 or -1, respectively. They change throughout the simulation to describe changes in spatial structure. A short-range attraction between like blocks and a long-range attraction between opposite blocks are two common interactions that can occur. By limiting domain expansion, they compete to promote microphase separation [66-69].
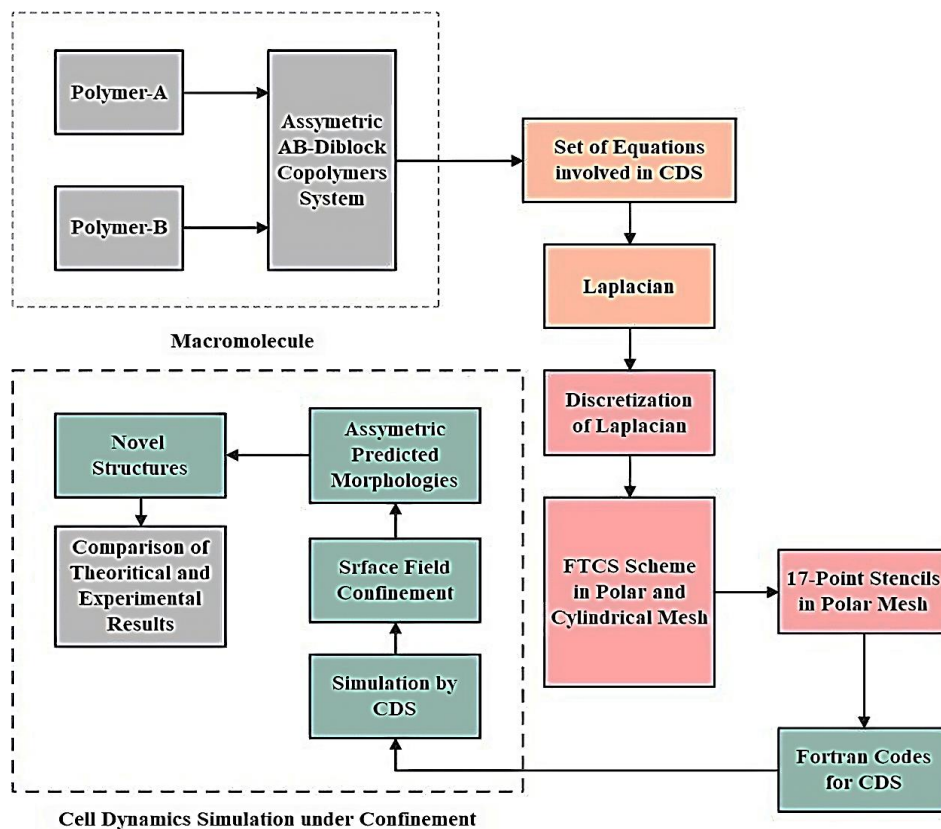

Figure 4: Algorithm of cell dynamics simulations

The flow chart of the CDS model is presented in Figure 4. In the initial stage, a continuum macromolecule of diblock copolymers consists of two polymer blocks. A 2D lattice is defined with periodic boundary conditions as the simulation domain and structure lattice-like 'cells' within this space. Random cell concentrations are generated based on the overall block concentrations. In the subsequent phase, the molecule is approximated for Laplacian, involved in the system, through isotropic discretization using a 17-point stencil in polar geometry. After converting all equations involved in the system, we produce FORTRAN code to run the simulation. The system's free energy is computed utilizing a formulation akin to Flory-Huggins, accounting for entropy, repulsive interactions, and chain stretching. Upon calculating the chemical potential at each lattice point based on this free energy formulation, dynamic steps are taken, invoking the Cahn-Hilliard dynamics equation to drive the system according to these chemical potentials.

A lattice cell and one of its neighbors are chosen randomly. The alteration in free energy, resulting from exchanging a small amount of material between the cells, is then computed. Following this, the exchange is carried out with a probability contingent upon the change in free energy. Concentration profiles, structure factors, domain sizes, and similar aspects are periodically outputted to facilitate self-assembly analysis. Confinement is introduced by imposing specific lattice site occupancy constraints. The simulation proceeds until a stable morphology is attained

2.2 Cell Dynamics Simulations

A diblock copolymer system consists of a macromolecule of two blocks A and B composed of N polymer chains. The length of each block is represented by N_α ($\alpha = A$ or $\alpha = B$) containing f_α monomers, α is a species of monomers in the form of $f_\alpha Z$ statistical segments with $l\, n^{\frac{1}{2}}$ scale length (l is Kuhn length). In the diblock copolymer system, the local volume fraction ϕ_α refers to the concentration of a block in a specific area of the material relative to the total volume. This parameter specifies how much of the block is in a particular region or material phase during simulation. In microphase separation, these two blocks are from distinct domains, and the spatial volume fraction helps to characterize these domains' size, shape, and distribution.

Theoretical models and simulations of diblock copolymers make it possible to account for local variations by local volume fraction in predicting the material's morphology, mechanics, and self-assembly behaviors. The global volume fraction is the total volume of the simulation box. It is defined in the initial setup of the simulation. It represents the overall size of the system and quantifies the overall properties of the system.

The local volume fractions are:

$$\phi_A = \frac{1}{\rho_0} \sum_{i=1}^{N} \int_0^{f_A} d\zeta \, \delta\{r - r_i^A(\zeta)\}. \tag{1}$$

$$\phi_B = \frac{1}{\rho_0} \sum_{i=1}^{N} \int_0^{f_B} d\zeta \, \delta\{r - r_i^B(\zeta)\}. \tag{2}$$

ρ_0 is density of melt and $r_i^\alpha(\xi)$ are chain conformations. The chain is parameterized by ζ with its length $0 < \zeta < N$ ($N = N_A + N_B$) and δ is an incompressibility constraint [70-71].

An order parameter $\psi(i,t)$ is found for cell i at time t in a discrete lattice cell dynamics simulation. The order ψ is computed for the AB diblock copolymer using the difference between the local and global volume fractions:

$$\psi = \phi_A - \phi_B + (1 - 2f) . \tag{3}$$

In (1), ϕ_A and ϕ_B are local volume fractions of A and B monomers respectively:

$$f = \frac{N_A}{N_A + N_B}. \tag{4}$$

Considering the difference between local and global volume fractions allows us to explore the spatial distribution of polymer chains, capture the effects of chain packing and interactions, and gain insights into the phase behaviour and self-assembly of diblock copolymer systems.

Any change in the order parameter over time must meet the requirements of the following equation to provide continuity:

$$\frac{\partial \psi(r,t)}{\partial t} = -\nabla \cdot j(r,t) \tag{5}$$

This equation assumes that $j(r,t)$ is a flux that is linearly connected to the local chemical potential:

$$j(r,t) = -M\nabla\mu(r,t) \tag{6}$$

The functional derivative of the free energy in the following way gives the chemical potential:

$$\mu(r,t) = \frac{\delta F[\psi]}{\delta \psi} \tag{7}$$

The Cahn-Hilliard-Cook (CHC) equation describes the order parameter's time evolution:

$$\frac{\partial \psi}{\partial t} = M\nabla^2\left(\frac{\delta F[\psi]}{\delta \psi}\right) + \eta\xi(r,t) \tag{8}$$

In this equation (5), $M = 1$ represents the mobility coefficient, η is the noise amplitude, and $\xi(r,t)$ is a Gaussian white noise with zero mean and unit variance. In this investigation, it is observed that $\eta\xi(r,t)$ does not significantly impact the simulation results. For this reason, the noise term is not programmed in the simulations.

In the derivation of the free energy, all the terms have a physical meaning. Even though the free energy is of course mesoscopic and coarse-grained and thus it is only an approximation [72].

The free energy functional $F[\psi(r)] \div kT$ is represented by the equation:

$$F[\psi(r)] = \int dr \left[H(\psi) + \frac{D}{2}|\nabla\psi|^2\right] + \left(\frac{B}{2}\right)\int dr \int dr' G(r - r')\psi(r)\psi(r') \tag{9}$$

$F[\psi(r)]$ has two terms. The first part $\int dr \left[H(\psi) + \frac{D}{2}|\nabla\psi|^2\right]$ of $F[\psi(r)]$ is identical to the Ginzburg–Landau free energy used to describe phase separation in a binary mixture. The

second part $F[\psi(r)]$ of $F[\psi(r)]$ represents the long-range interactions arising from the connectivity of different blocks in a copolymer [73].

D is a positive constant for the diffusion coefficient. $G(r - r')$ is a green function for Laplacian, satisfies $\nabla^2 G(r - r') = -\delta(r - r')$ [36].

The parameter B introduces a chain-length dependence on the free energy $H(\psi)$ [74], given as

$$H(\psi) = \left[\left(-\frac{\tau}{2}\right) + \left(\frac{A}{2}\right)(1 - 2f)^2\right]\psi^2 + v(1 - 2f)\psi^3 + \left(\frac{u}{4}\right)\psi^4 \qquad (10)$$

The temperature parameter is represented by τ, while A v, and u are phenomenological constants. $\tau' = -\tau + A(1 - 2f)^2, D,$ and B can be expressed in terms of the degree of polymerization N, the segment length b, and the Flory-Huggins parameter χ, which is inversely proportional to temperature. The χ-parameter is used to measure the relative strength of the repulsion $(\chi > 0)$ and attraction $(\chi < 0)$ between the same types of segments. The expressions for τ', D, and B are given by:

$$\tau' = \left(-\frac{1}{2N}\right)\left(N\chi - \frac{s(f)}{4f^2(1-f)^2}\right) \qquad (11)$$

$$D = \frac{b^2}{48f(1-f)} \qquad (12)$$

$$B = \frac{9}{4N^2b^2f^2(1-f)^2} \qquad (13)$$

Numerical evolution of CDS equation (2) by finite difference scheme for order parameter is given below.

$$\psi(\boldsymbol{n}, t + 1) = \psi(\boldsymbol{n}, t) - \{\langle\langle\Gamma(\boldsymbol{n}, t)\rangle\rangle - \Gamma(\boldsymbol{n}, t)\} + B\psi(\boldsymbol{n}, t) - \eta\xi(\boldsymbol{n}, t). \qquad (14)$$

Where $\Gamma(\boldsymbol{n}, t) = g(\psi(\boldsymbol{n}, t)) - \psi(\boldsymbol{n}, t) + D[\langle\langle\psi(\boldsymbol{n}, t)\rangle\rangle - \psi(\boldsymbol{n}, t)]. \qquad (15)$

$\{\langle\langle\Gamma(\boldsymbol{n}, t)\rangle\rangle\} - \Gamma(\boldsymbol{n}, t)$ is isotropized discrete Laplacian [38] in polar and $i = (i_r, i_\theta)$ are polar coordinates with Δt time steps for order parameters.

In case of confinement

$$\Gamma(n, t) = g(\psi(n, t)) - \psi(n, t) + D[\langle\langle\psi(n, t)\rangle\rangle - \psi(n, t)] - s_i(r). \qquad (16)$$

Here $s_i(r) = h_i \times \emptyset_i \times \delta_{n_r=1 \text{ or } n_r=N_r}.$

The strength of the mutual interaction of walls and blocks is h_i. The Kronecker delta, represented by $\delta_{n_r=1 \text{ or } n_r=N_r}$. This equation is the product of the total segments h_i, the local volume fraction $\emptyset_i$, and the Kronecker delta function $\delta_{n_r=1 \text{ or } n_r=N_r}$. This equation is used to calculate the local segment density at the r position of the specified i block. The Kronecker delta function ensures that the fractional density contribution comes only from cells at the boundaries of the system $(n_r = 1 \text{ or } n_r = N_r)$, so that these cells are more likely to be interfaces or boundaries between different blocks.

The discretization of the free energy function $g(\psi)$ is given by:

$$g(\psi) = [1 + \tau - A(1 - 2f)^2]\psi - v(1 - 2f)\psi^2 - u\psi^3. \qquad (17)$$

We know the Laplacian in polar form

$$u_{rr} + \frac{1}{r}u_r + \frac{1}{r^2}u_{\theta\theta} = \nabla^2 \tag{18}$$

Here we take $0 \leq \theta \leq 2\pi$ with $\theta_j = j\Delta\theta$ for $i = 1,2,3,\dots,n_r$ and $r_a \leq r \leq r_b$ with $r_i = r_a + i\Delta r$ for $j = 1,2,3,\dots,n_\theta$. The finite difference approach for the Laplacian used in the CDS model in the polar mesh accomplishes the discretization of a continuum molecule of the diblock copolymer system into discrete set-off points. Periodic boundary conditions are applied to the radian domain, reflective boundary conditions are applied to the radian domain, and symmetric boundary conditions are applied to the confinement domain.

2.3 The Isotropic Formulation of $\langle\langle\Gamma(n,t)\rangle\rangle - \psi(n,t)$

In a polar grid, the Laplacian operator ∇^2 exhibits a distinct structure compared to Cartesian coordinates due to the incorporation of radial and angular variables (r, θ). To approximate the second-order partial derivatives of the Laplacian, a finite difference stencil is employed. Achieving an isotropic and rotationally invariant approximation in the polar grid requires a 17-point stencil. These 17 points comprise the central point (i,j), six immediate neighboring points along the radial direction, six neighboring points along the angular direction, and four mixed neighboring points. These points will be approximated for radial and radian rates of change. The macromolecule of diblock copolymers in the form of 17 discrete points is shown in Figure 5.

First-order approximation of the partial derivative for the 3 points $(i-1, j+1)$, $(i, j+1)$ and $(i+1, j+1)$ along the radial axis, given as:

$$\psi_r = \frac{1}{2(\Delta r)}\{\psi_{i+1,j+1} - \psi_{i-1,j+1}\}. \tag{19}$$

First-order approximation of the partial derivative for the 7 points $(i-3,j)$, $(i-2,j)$, $(i-1,j)$, (i,j), $(i+1,j)$, $(i+2,j)$ and $(i+3,j)$ along the radial axis, given as:

$$\psi_r = \frac{1}{60(\Delta r)}\{-\psi_{i-3,j} + 9\psi_{i-2,j} - 45\psi_{i-1,j} + 45\psi_{i+1,j} - 9\psi_{i+2,j} + \psi_{i+3,j}\} \tag{20}$$
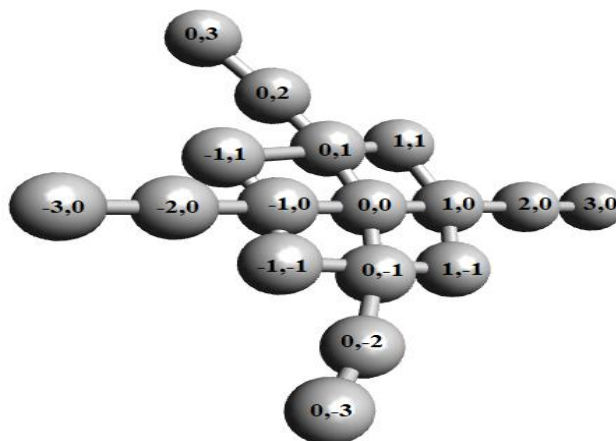

Figure 5: 17-Point discrete molecule of diblock copolymers system

First-order approximation of the partial derivative for the 3 points $(i-1, j-1)$, $(i, j-1)$ and $(i+1, j-1)$ along the radial axis, given as:

$$\psi_r = \frac{1}{2(\Delta r)}\{\psi_{i+1,j-1} - \psi_{i-1,j-1}\}. \tag{21}$$

Adding (19), (20) and (21), we get the first-order approximations of the partial derivatives along the radial axis, given as:

$$\psi_r = \frac{1}{180(\Delta r)}[\{-\psi_{i-3,j} + 9\psi_{i-2,j} - 45\psi_{i-1,j} + 45\psi_{i+1,j} - 9\psi_{i+2,j} + \psi_{i+3,j}\} + 30\{\psi_{i+1,j+1} - \psi_{i-1,j+1}\} + 30\{\psi_{i+1,j-1} - \psi_{i-1,j-1}\}]. \tag{22}$$

Second-order approximation of the partial derivative for the 3 points $(i-1, j+1)$, $(i, j+1)$ and $(i+1, j+1)$ along the radial axis, given as:

$$\psi_{rr} = \frac{1}{(\Delta r)^2}\{\psi_{i+1,j+1} - 2\psi_{i,j+1} + \psi_{i-1,j+1}\} \tag{23}$$

Second-order approximation of the partial derivative for the 7 points $(i-3, j)$, $(i-2, j)$, $(i-1, j)$, (i, j), $(i+1, j)$, $(i+2, j)$ and $(i+3, j)$ along radial axis, given as.

$$\psi_{rr} = \frac{1}{180(\Delta r)^2}\{2\psi_{i-3,j} - 27\psi_{i-2,j} + 270\psi_{i-1,j} - 490\,\psi_{i,j} + 270\psi_{i+1,j} - 27\psi_{i+2,j} + 2\psi_{i+3,j}\} \tag{24}$$

order approximation of the partial derivative for the 3 points $(i-1, j-1)$, $(i, j-1)$ and $(i+1, j-1)$ along the radial axis, given as.

$$\psi_{rr} = \frac{1}{(\Delta r)^2}\{\psi_{i+1,j-1} - 2\psi_{i,j-1} + \psi_{i-1,j-1}\} \tag{25}$$

Adding (23), (24), and (25) gives the second-order approximations of the partial derivatives along the radial axis, given as.

$$\psi_{rr} = \frac{1}{540(\Delta r)^2}[\{2\psi_{i-3,j} - 27\psi_{i-2,j} + 270\psi_{i-1,j} - 490\,\psi_{i,j} + 270\psi_{i+1,j} - 27\psi_{i+2,j} + 2\psi_{i+3,j}\} + 180\{\psi_{i+1,j-1} - 2\psi_{i,j-1} + \psi_{i-1,j-1}\} + 180\{\psi_{i+1,j+1} - 2\psi_{i,j+1} + \psi_{i-1,j+1}\}] \tag{26}$$

Second-order approximation of the partial derivative for the 3 points $(i-1, j+1)$, $(i-1, j)$ and $(i-1, j-1)$ along the radian axis, given as.

$$\psi_{\theta\theta} = \frac{1}{(\Delta\theta)^2}\{\psi_{i-1,j+1} - 2\psi_{i-1,j} + \psi_{i-1,j-1}\} \tag{27}$$

Second-order approximation of the partial derivative for the 7 points $(i, j-3)$, $(i, j-2)$, $(i, j-1)$, (i, j), $(i, j+1)$, $(i, j+2)$ and $(i, j+3)$ along radial axis, given as.

$$\psi_{\theta\theta} = \frac{1}{180(\Delta\theta)^2}\{2\psi_{i,j-3} - 27\psi_{i,j-2} + 270\psi_{i,j-1} - 490\,\psi_{i,j} + 270\psi_{i,j+1} - 27\psi_{i,j+2} + 2\psi_{i,j+3}\} \tag{28}$$

Second-order approximation of the partial derivative for the 3 points $(i+11, j+1)$, $(i+1, j)$ and $(i+1, j-1)$ along the radian axis, given as.

Second-order approximation of the PDE for the points given in Figure 2.9, along the radial axis, given as:

$$\psi_{\theta\theta} = \frac{1}{(\Delta\theta)^2}\{\psi_{i+1,j+1} - 2\psi_{i+1,j} + \psi_{i+1,j-1}\} \tag{29}$$

Adding (27), (28) and (29), we get.

$$\psi_{\theta\theta} = \frac{1}{540(\Delta\theta)^2}\{2\psi_{i,j-3} - 27\psi_{i,j-2} + 270\psi_{i,j-1} - 490\,\psi_{i,j} + 270\psi_{i,j+1} - 27\psi_{i,j+2} +$$
$$2\psi_{i,j+3}\} + 180\{\psi_{i-1,j+1} - 2\psi_{i-1,j} + \psi_{i-1,j-1}\} + 180\{\psi_{i+1,j+1} - 2\psi_{i+1,j} + \psi_{i+1,j-1}\} \quad (30)$$

Now for the approximation of Laplacian involved in the CDS model, we put (22), (26) and (30) in (18) and get.

$$\nabla^2_\psi = \frac{1}{540(\Delta r)^2}\Big[\{2\psi_{i-3,j} - 27\psi_{i-2,j} + 270\psi_{i-1,j} - 490\,\psi_{i,j} + 270\psi_{i+1,j} - 27\psi_{i+2,j} + 2\psi_{i+3,j}\}$$
$$+ 180\{\psi_{i+1,j-1} - 2\psi_{i,j-1} + \psi_{i-1,j-1}\} + 180\{\psi_{i+1,j+1} - 2\psi_{i,j+1} + \psi_{i-1,j+1}\}\Big]$$
$$+ \frac{1}{180(r\Delta r)}\Big[\{-\psi_{i-3,j} + 9\psi_{i-2,j} - 45\psi_{i-1,j} + 45\psi_{i+1,j} - 9\psi_{i+2,j} + \psi_{i+3,j}\}$$
$$+ 30\{\psi_{i+1,j+1} - \psi_{i-1,j+1}\} + 30\{\psi_{i+1,j-1} - \psi_{i-1,j-1}\}\Big]$$
$$+ \frac{1}{540(r\Delta\theta)^2}\{2\psi_{i,j-3} - 27\psi_{i,j-2} + 270\psi_{i,j-1} - 490\,\psi_{i,j} + 270\psi_{i,j+1} - 27\psi_{i,j+2}$$
$$+ 2\psi_{i,j+3}\} + 180\{\psi_{i-1,j+1} - 2\psi_{i-1,j} + \psi_{i-1,j-1}\} + 180\{\psi_{i+1,j+1} - 2\psi_{i+1,j}$$
$$+ \psi_{i+1,j-1}\}$$

Implies

$$\langle\langle\Gamma(n,t)\rangle\rangle - \psi(n,t) = \omega \sum_{i=1}^{n_r}\sum_{j=1}^{n_\theta}\Big[\Big\{\frac{1}{540(\Delta r)^2}\{2\psi_{i-3,j} - 27\psi_{i-2,j} + 270\psi_{i-1,j} + 270\psi_{i+1,j} - 27\psi_{i+2,j} +$$
$$2\psi_{i+3,j}\} + \frac{1}{3(\Delta r)^2}\{\psi_{i+1,j+1} - 2\psi_{i,j+1} + \psi_{i-1,j+1} + \psi_{i+1,j-1} - 2\psi_{i,j-1} + \psi_{i-1,j-1}\}\Big\} + \frac{1}{r}\Big\{\frac{1}{180(\Delta r)}\{-\psi_{i-3,j} +$$
$$9\psi_{i-2,j} - 45\psi_{i-1,j} + 45\psi_{i+1,j} - 9\psi_{i+2,j} + \psi_{i+3,j}\} + \frac{1}{6(\Delta r)}\{\psi_{i+1,j+1} - \psi_{i-1,j+1} + \psi_{i+1,j-1} - \psi_{i-1,j-1}\}\Big\} +$$
$$\frac{1}{r^2}\Big\{\frac{1}{540(\Delta\theta)^2}\{2\psi_{i,j-3} - 27\psi_{i,j-2} + 270\psi_{i,j-1} + 270\psi_{i,j+1} - 27\psi_{i,j+2} + 2\psi_{i,j+3}\} + \frac{1}{3(\Delta\theta)^2}\{\psi_{i+1,j+1} +$$
$$\psi_{i-1,j-1} + \psi_{i-1,j+1} + \psi_{i+1,j-1} - 2\psi_{i+1,j} - 2\psi_{i-1,j}\}\Big\}\Big] - \sum_{i=1}^{n_r}\sum_{j=1}^{n_\theta}\psi_{i,j} \quad (31)$$

Here, the waiting factor for neighboring nearest neighboring points is $\omega = \left[\frac{54(r\Delta r\Delta\theta)^2}{49\{(\Delta r)^2 + (r\Delta\theta)^2\}}\right]$

In this numerical scheme, i is taken as a discrete variable for radial step and j is taken as a discrete variable representing an angular step in a polar grid system. However, $r_i \in \mathcal{R}$ and $\theta_j \in \mathcal{R}$. For pore size, $d = |r_a - r_b|$, r_a is the interior radius of the disc and r_b is the exterior radius of the disc. The interior radius is set to fix at $r_a = 3$ or $r_a = 5$ or $r_a = 7$ to avoid issues of singularities and the size r_b varies according to the size of the pore.

3. SIMULATIONS RESULTS

The primary objective of the simulation is to enhance our understanding of phase separation and compositional control. We examine diblock copolymer systems within annular circular pores of varying sizes to attain this goal. Employing polar grids for discretizing the diblock copolymer system and envisioning diverse patterns within the annular circular pores, we conduct simulations of the diblock copolymer system using the

CDS model in this study. The outcomes from the 2D computational analysis serve to identify key variables and constraints influencing morphological control within constrained geometries. This paper explores two-dimensional computational simulations of diblock copolymers using polar coordinates within circular annular pores. We model different pore shapes and sizes, encompassing lamellae, cylinders, and spheres. The findings offer insights for three-dimensional investigations, shedding light on phase separation and morphological control within a confined two-dimensional domain. The simulations employ reflective boundary conditions along the radial axis, utilizing $\Delta r = 0.1$ and $\Delta t = 0.1$. Within the domain $0 \leq \theta \leq 2\pi$, periodic boundary conditions are implemented by setting $\Delta \theta = 0.017453292$. The simulation is bifurcated into two categories: first, studying the binary fluid, and second, simulating the creation of lamellar, cylindrical, and spherical shapes within pore systems, both with and without confinement.

3.1 Binary Fluid simulation and predictions

We simulate a binary fluid inside a system of annular circular discs. Instead of treating this mixture as a self-assembling diblock copolymer, we model it as two fluids devoid of interaction. Binary fluid simulations in pore geometry serve as a test case to validate our computational method, confirming the expected occurrence of macrophase separation in a simple mixture without microphase separation or self-assembly.

Table 1: CDS parameters for binary fluid

A	B	D	u	v	f	τ	Time steps
1.50	0	0.70	0.38	2.30	0.48	0.36	1000000

The parameter B is responsible for the self-organization of diblock copolymers into microstructures and microphase separation. The parameter is set $B = 0$ to get macrophase separation instead of microphase separation.
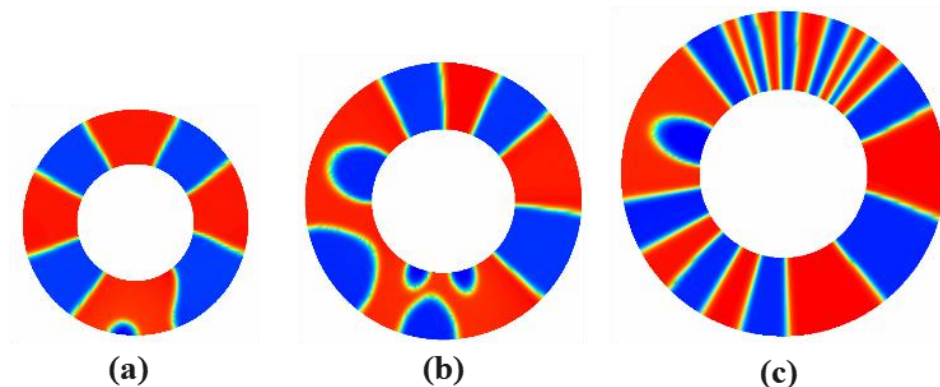

(a) (b) (c)

Figure 6: **Binary fluid system at one million-time steps with internal radius (a) $r_a = 3$, (b) $r_a = 5$, (c) $r_a = 7$ and pore size $d = 2$**

We simulate the program to a one-million-time step and predict the result of the simulation that the continuum molecule of the diblock copolymers system is equally distributed between two subdomains, red-rich (polymer A) and blue-rich (polymer B).

3.2 Asymmetric Lamellae forming simulation with neutral walls

In the second phase of the simulation, we analyze the morphology of asymmetric lamellae ($f_a \neq f_b$) within a diblock copolymer system arranged in a circular-annular disc. This study investigates diverse pore sizes employing a coarse-grained simulation approach. For this purpose, the global volume fraction is set at $f_A = 0.48$, $f_B = 0.52$ and temporal parameter $\tau = 0.36$. Table 3.2 shows all parameters and their values used in the CDS model to computationally model the asymmetric lamella forming system.

Table 2: Simulation parameters for asymmetric Lamellae in polar discs with neutral walls

A	B	D	u	v	f	τ	α	Time steps
1.50	0.02	0.70	0.38	2.30	0.48	0.36	0	1000000

The simulation results for Lamellae forming systems in annular discs are obtained by increasing the pore size, achieved by varying the outer pore radius r_b while keeping the inner pore radius r_a fixed at 3.
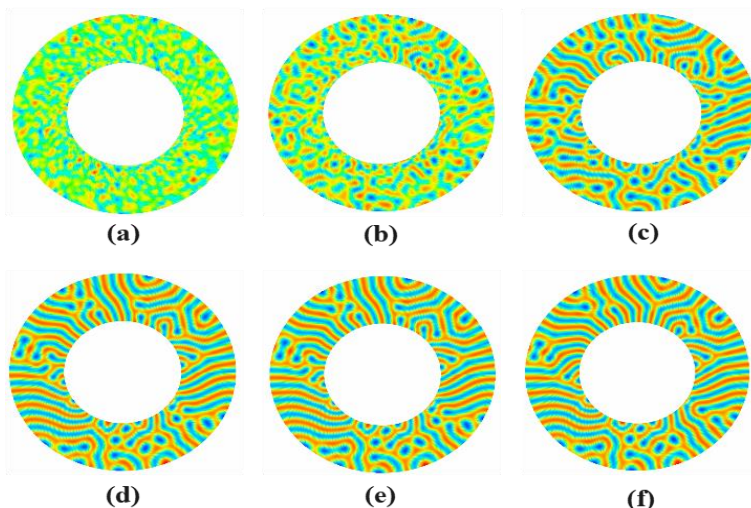
Figure 7: Lamellae forming system at various time steps, including t=10 in (a), t=100 in (b), t=1000 in (c), t=10000 in (d), t=100000 in (e), and t=1000000 in (f)

Figure 7 illustrates the simulation of the Lamellae forming system with a grid size of 30×60 by setting internal radius $r_a = 3$, external radius $r_b = 6$, and pore size $d = 3$. The natural inclination to minimize interfacial energy between the immiscible blocks is the driving force behind the formation of lamellar domains in the diblock copolymer within the confines of the annular pore. In the initial time steps, discrete domains didn't form, and the blocks remained disordered and mixed due to their chemical incompatibility. However, as the simulation progressed, the blocks began to phase-separate, arranging into distinct phases to achieve a lower energy state. The lamellar domains gradually oriented perpendicular to the pore walls during this process. As the simulation moved through intermediate time steps, the blocks further rearranged, forming more ordered domains, causing the lamellae to expand in thickness and width. In the later time steps, well-defined

and organized lamellar domains emerged, clearly demarcating the A and B blocks. Eventually, the system reached an equilibrium state, characterized by alternating A and B lamellae spanning the annular pores, forming an ordered configuration and occupying the available space. Various factors, including the relative volume fractions of the blocks, pore size, and the strength of interactions between the blocks and the pore walls influenced the thickness and number of lamellae formed.
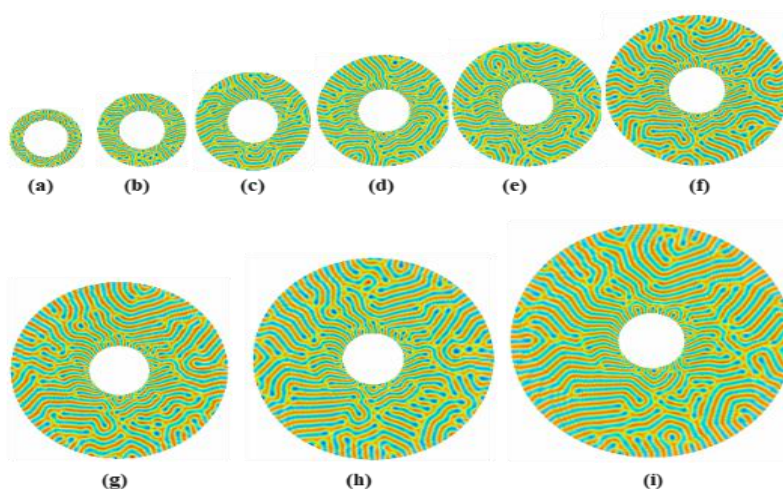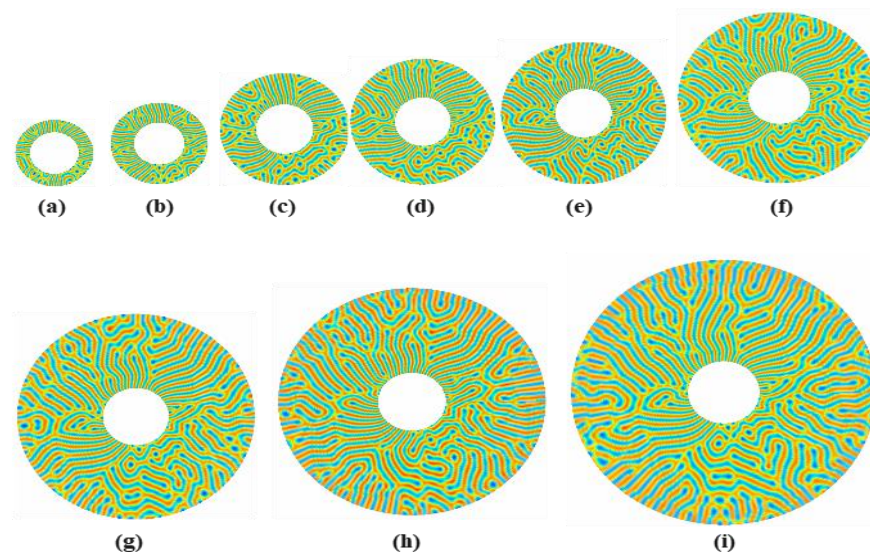

Figure 8: Lamellae forming system in circular annular discs with neutral walls at $r_a = 3$ with pore size $d = 2$ in (a), $d = 3$ in (b), $d = 4$ in (c), $d = 5$ in (d), $d = 6$ in (e), $d = 7$ in (f), $d = 8$ in (g), $d = 9$ in (h) and $d = 10$ in (i)

In Figure 8, Investigations are made into the lamellar morphology of the asymmetric DBC system in the annular disc with the size of the pore $d = 2,3,4,5,6,7,8,9$, and 10. The pore's internal radius, $r_a = 3$, and its outward radii r_b, vary from 5 to 13. Figure 8 shows the simulation results of an asymmetric diblock copolymer system in a circular annular pore. A look at pore size $d = 2$, shows that we have *y*-shaped and *v*-shaped lamellae parallel to the radial axes of the pore with some single lamellae strips between them. Some perforations are also visible near the inner circumference of the pore. In pore size $d = 3$ the deformation process begins and perforated holes and *u*-shaped lamellae are seen changing into y-shaped Lamellae.

Parallel stripes form on the right and left sides of the disc, and an increase in the frequency of perforations is observed in the lower half of the disc. An Increase in pore size to $d = 4$ zigzag-shaped lamellae due to distortion in a perforated hole. Lengthened and skewed *y*-lamellae and alternating *v*-lamellae are prominent in pore size $d = 5$. As the pore size increases from 5 to 6,7,8,9 and 10, the length of different lamella patterns and their skewness also increase. An increase can be seen in perforated holes with an increasing number of parallel stripes near the inner and outer walls of the pore due to deformation and formation along tilted curved strips. Some dimples are also present. We can see open-ended parallel strips in bigger pore sizes. Some holes, oblique ridges, oblique longitudinal *y*-shaped lamellae, and alternating *u* and *y* lamellae are seen between them.

Figure 9: Lamellae forming system in circular annular discs with neutral walls at $r_a = 5$ in pore size d = 2 in (a), d = 3 in (b), d = 4 in (c), d = 5 in (d), d = 6 in (e), d = 7 in (f), d = 8 in (g), d = 9 in (h) and d = 10 in (i)

The lamellar morphology of the asymmetric diblock copolymers (DBC) system in the annular disc with pore size $d = 2,3,4,5,6,7,8,9,$ and 10 is investigated in figure 9. The pore's internal radius, $r_a = 5$, and its outer radius, r_b, ranges from $7, 8, 9, 10, 11, 12, 13, 14$ to 15. In pore size 2, parallel stripes with y-shaped lamellae are observed in the upper half of the disc In the lower half, the same stripes are interspersed with u-type patterns, and some holes are also clearly visible.

By increasing the pore size to 3, the deformation of the perforated forms longitudinal stripes. Also, the y and reflected y patterns converge, with a linear band appearing in the middle. By increasing the pore size to 4, parallel strip lamellae form in the disc's upper and lower halves.

The deformation of perforated holes finds dimple-like patterns. The number of perforated holes also increases in the disc's lower half. Due to the polar geometry, increasing distortion in pore sizes 5, 6, and 7 results in forming new perforated holes along with skewness in the parallel stripes. Some y-rays and reflected y-rays are seen together, with u- and v-patterns forming on the inner and outer sides of the pore.

Figure 10 shows investigations into the lamellar morphology of asymmetric diblock copolymers (DBC) system in an annular disc with diameters of pore $d = 2,3,4,5,6,7,8,9,$ and 10. The pore's internal radius, $r_a = 7$, and its outer radius r_b, can range from $9, 10, 11, 12, 13, 14, 15,$ and 16 to 17. Looking at the simulation results, the disc pore size 2 shows parallel stripes and a y pattern between them. Looking at the simulation results, pore size 2 of the disc shows parallel stripes and a y pattern between them.
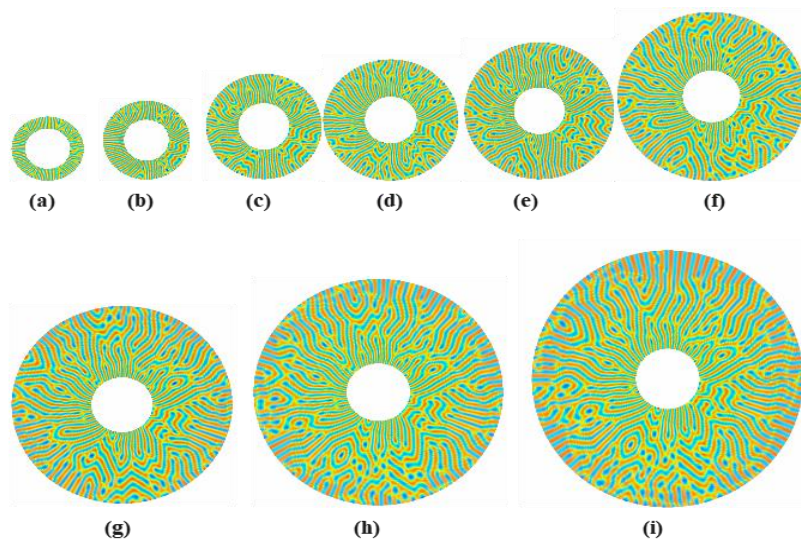
Figure 10: Lamellae forming system in circular annular discs with neutral walls at $r_a = 7$ **in pore size d $= 2$ in (a), d $= 3$ in (b), d $= 4$ in (c), d $= 5$ in (d), d $= 6$ in (e), d $= 7$ in (f), d $= 8$ in (g), d $= 9$ in (h) and d $= 10$ in (i)**

These parallel strips are accompanied by V patterns and y and reflected y pairs patterns. At pore size 3, the v pattern combined with a single stripe gives a w morphology. The reflected y morphology and the single stripe appear to form a H-type pattern. Due to the effect of curvature, perforated holes begin to form, which seem to increase in number with increasing pore size. At pore size 4 of the disc, the radial stripes on the upper half and lower half appear to change to wavy stripes with elongated y-patterns in between. Also prominent are the u and v patterns. At pore size 5, m-shaped patterns increase in length and parallel stripes change to curved stripes. At pore size 6, we see smaller parallel strips joining a longitudinal strip. The outer wall appears to be u-shaped and parallel strips are formed near the inner wall. At pore sizes 7, 8, 9 and 10, u and y-type patterns are prominent along the inner and outer walls, while mixed patterns are observed in the middle, which increases in length with increasing pore size. They also have skewness due to curvature.

3.3 Asymmetric Lamellae forming simulation with Attractive walls

In this simulation phase, the encapsulation of diblock polymers into circular annular pores significantly distorts the microdomain structure by attractive interactions between a block and the pore walls. The main reason for this is surface affinity. The interactive strength dependence is expressed as a parameter α, the higher the value, the higher the surface strength.

Table 3: Simulation parameters for asymmetric Lamellae in polar discs with attractive walls

A	B	D	u	v	f	τ	α	Time steps
1.50	0.02	0.70	0.38	2.30	0.48	0.36	0.2	1000000

The volume fraction of Block A is set at $f = 0.48$ and a parameter $\alpha = 0.2$ for the surface affinity of asymmetric diblock copolymers confined in annular circular pores. As the surface preference strength increases from zero to 0.2, the morphology evolves through various stages to form a tilted lamellar pattern along the walls. Moreover, at this high surface preference, morphologies, including rings, toroids, and labyrinth patterns, can emerge depending on the relative volume fractions and pore size. The ratio of the copolymer radius of gyration to pore size affects the ability to shape under confinement. A higher ratio allows for more traditional structures.

Figure 11 shows the simulation results of an annular circular pore for an asymmetric diblock copolymer system with attractive walls ($\alpha = 0.2$). The inner radius r_a is 3 and the outer radii r_b are 5, 6, 7, 8, 9, 10, 11, 12 and 13 according to the pore sizes $d = 2, 3, 4, 5, 6, 7, 8, 9$ and 10. In the simulation results at pore size 2, perforated holes are observed and dumbbells formed by these holes and parallel stripes in the disc in the radian domain. At pore size 3, dumbbell patterns appear to change to vertical diagonal stripes, and perforated pores appear to increase. Pore size 4 shows an increase in vertical tilted stripes in the upper and lower halves of the disk. At pore size 5, deformation of the dumbbells and stripes causes parallel stripes, which converge near one end, leading to w and y pattern shapes. At pore size 6, a m-shaped morphology is obtained, and new perforated holes appear to form. Increasing the pore size further to 8,9 and 10, results in longitudinal and oblique y, u, w patterns. Perforated holes are seen to transform into open-ended strips, and new holes are also seen to form due to increased curvature and confinement strength leading to new equilibrium phases.
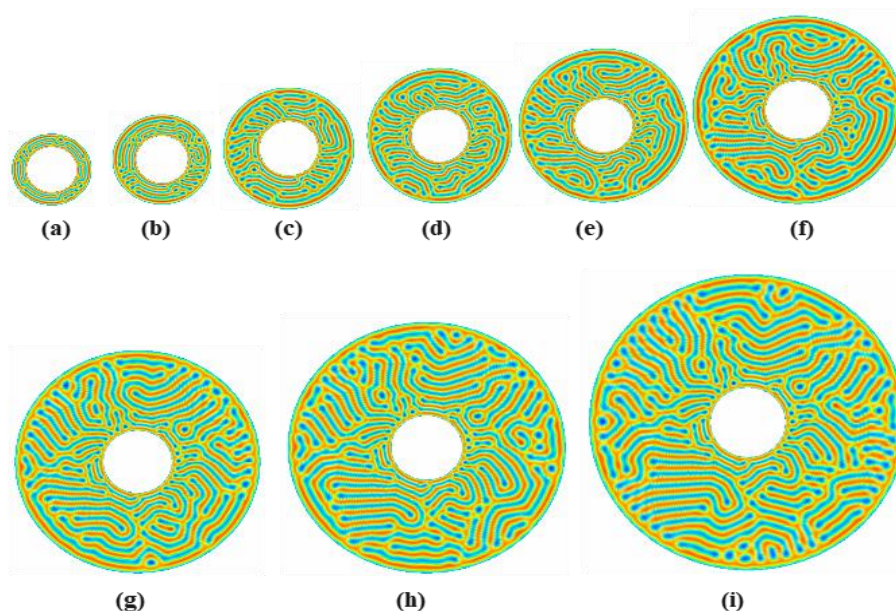

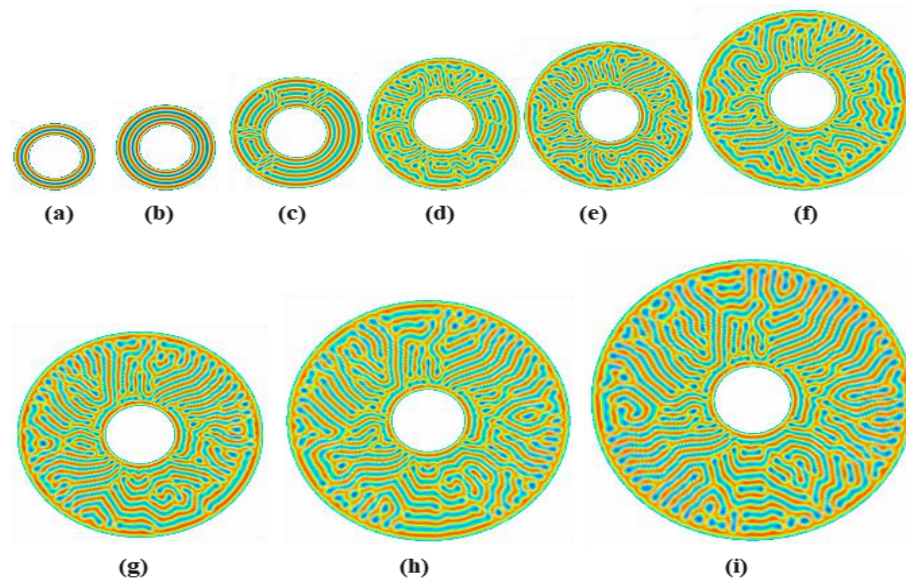**Figure 11: Lamellae forming system in circular annular discs with attractive walls at $r_a = 3$ in pore size d = 2 in (a), d = 3 in (b), d = 4 in (c), d = 5 in (d), d = 6 in (e), d = 7 in (f), d = 8 in (g), d = 9 in (h) and d = 10 in (i)**

The modelling results of an annular circular pore for an asymmetric diblock copolymer system with attractive walls ($\alpha = 0.2$) are shown in Figure 12. The pore size d is 2, 3, 4, 5, 6, 7, 8, 9 and 10, the inner radius r_a is 5 and the outer radii r_b are 7, 8, 9, 10, 11, 12, 13, 14 and 15. At pore sizes 2 and 3, the concentric circles are obtained.

Increasing the pore size to 4 increases the curvature, and increasing the degree of segregation causes deformation of these concentric circles. Bands parallel to the pore appear to split into pieces, and some bands parallel to the radial axes appear to form.

Perforated holes are found at pore size 5, and dumbbell-type specimens gradually increase. Due to the effects of curvature and confinement, the patterns formed in the angular domain appear skewed in the radial domain. Perforated holes at pore size 6 and dumbbells form y-patterns due to mechanical deformation with longitudinally elongated patterns.

At pore size 7, the y pattern deforms and meets the open-ended lamellae, forming a mixed w pattern. At pore sizes 8, 9 and 10, due to the increase of inner radius, confinement strength and curvature effects, oblique lamellar y and w patterns are seen with diagonally parallel stripes of lamellae.

Figure 12: Lamellae forming system in circular annular discs with attractive walls at $r_a = 5$ in pore size $d = 2$ in (a), $d = 3$ in (b), $d = 4$ in (c), $d = 5$ in (d), $d = 6$ in (e), $d = 7$ in (f), $d = 8$ in (g), $d = 9$ in (h) and $d = 10$ in (i)

These lamellae are distinct on the outer and inner sides of the disc, while mixed patterns are seen between these walls.
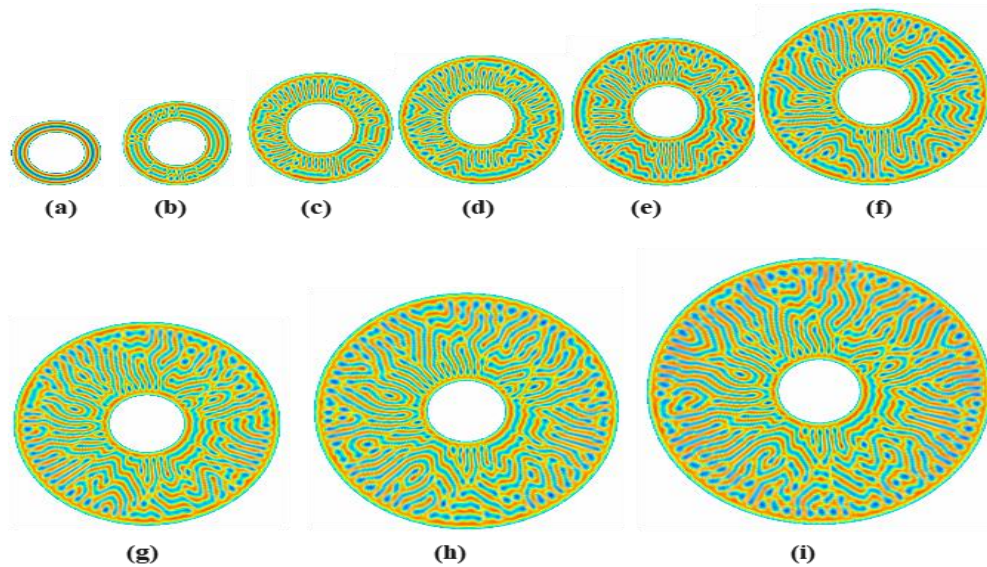
Figure 13: Lamellae forming system in circular annular discs with attractive walls at $r_a = 7$ in pore size   d = 2 in (a), d = 3 in (b), d = 4 in (c), d = 5 in (d), d = 6 in (e), d = 7 in (f), d = 8 in (g), d = 9 in (h) and d = 10 in (i)

The modelling results of an annular circular pore for an asymmetric diblock copolymer system with attractive walls ($\alpha = 0.2$) are shown in Figure 13. According to the d pore size 2, 3, 4, 5, 6, 7, 8, 9 and 10, the fixed internal radius of the pore is $r_a = 7$, the outer radii of the pore are 7, 8, 9, 10, 11,12,13,14,15,16 and 17. At pore size 2, concentric circles are observed, which deform into pore-parallel and vertical stripes at pore size 3. Microporous pores are also found. As the curvature increases at pore size 4, these porous pores are seen to deform into longitudinally growing dumbbells and lamellas parallel to the radial axes. Some vortices also appear and an increase in the frequency of holes is observed. At pore size 5, y-patterns are found along with long loops changing to m-patterns. Some y-patterns are also fseen and the frequency of holes increases. At pore size 6, y-patterns are combined with long stripes, changing to m-patterns. At pore size 7, the old perforated holes deform and intersect the y-lamellae and form new M-lamellae. The strips increase in length and form a curve shape but elongate in size. Some alternating v patterns can be seen. Due to the rise in inner radius, confinement strength, and curvature effects, oblique, lamellar y and w patterns with diagonally parallel lamellae stripes can be visible at pore sizes 8, 9, and 10. On the outer and inner edges of the disc, these lamellae are distinct, and between these walls, mixed patterns can be seen. Some dumbbell patterns and tilda patterns are also available.

3.4 Cylindrical forming simulation with neutral walls

In this phase of simulation, Diblock copolymer cylindrical morphology is studied in circular annular nano disc without geometric confinement in one and two dimensions. The pore geometry simulation produced results after one million time steps. Table 3.4 shows the parameters and their values for the cylindrical forming system.

Table 4: Cylindrical morphologies in polar discs with neutral walls $at\ r_a = 3$

A	B	D	u	v	f	τ	r_a	α
1.50	0.02	0.50	0.58	1.50	0.40	0.30	3	0

The inner pore radius is set at 3, and the outer pore radius is varied to increase the pore size in diblock copolymer lamellae-forming systems in annular circular discs. Figure 14 depicts the cell dynamic simulation for the cylindrical forming system with a grid size of $30 \times 60 \times 1$ ($r_a = 3$), external radius $r_b = 6$, and pore size $d = 3$. As the domains continue to grow and orient symmetrically throughout the film thickness, a hexagonal packing of cylinders develops.
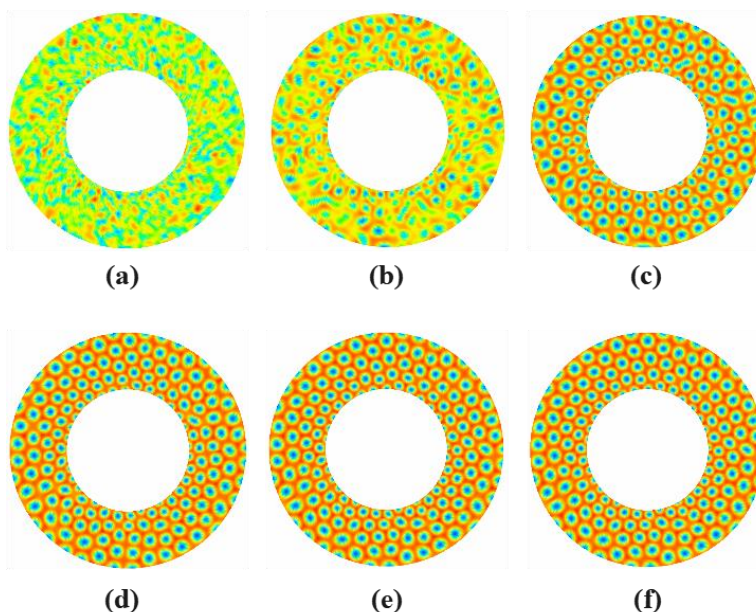
Figure 14: Cylindrical forming system at various time steps, including t=10 in (a), t=100 in (b), t=1000 in (c), t=10000 in (d), t=100000 in (e), and t=1000000 in (f)

The simulation results of the cylindrical morphology in an annular circular disk for neutral walls are shown in Figure 15. The study is done on the pore sizes d= 2, 3, 4, 5, 6, 7, 8, 9 and 10, set $r_a = 3$ and the outer radius r_b are 5, 6, 7, 8, 9, 10, 11, 12 and 13. Cylindrical systems indicate that the microdomains align with logarithmic spiral lines within the pores in terms of pore geometry.

Furthermore, within this geometric design, the microdomains adopt a hexagonal packing configuration. Cylinders in the system are shown with pore size d = 2 and are located on the logarithmic spiral lines close to the origin. As the pore size increases, these logarithmic spiral lines become wider. This reflects the effect of geometry caused by the increasing pore size s of the annular circular disc.
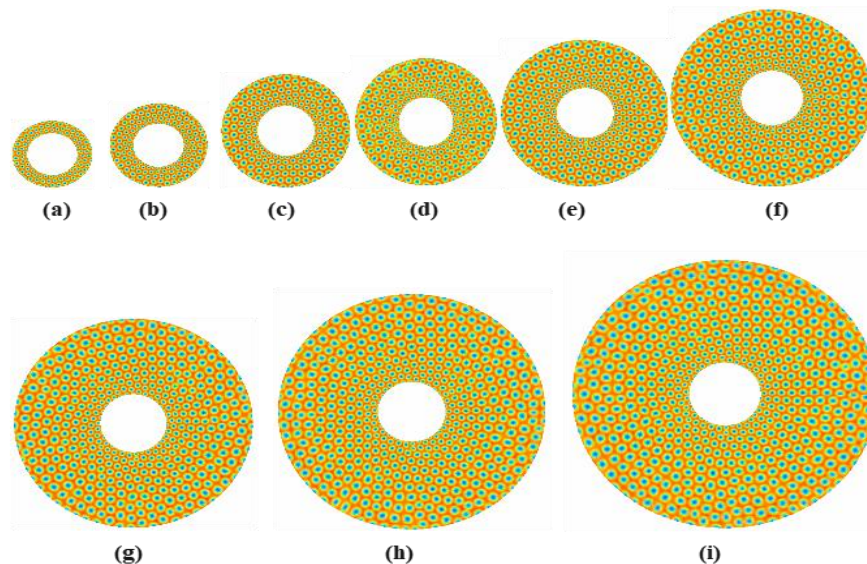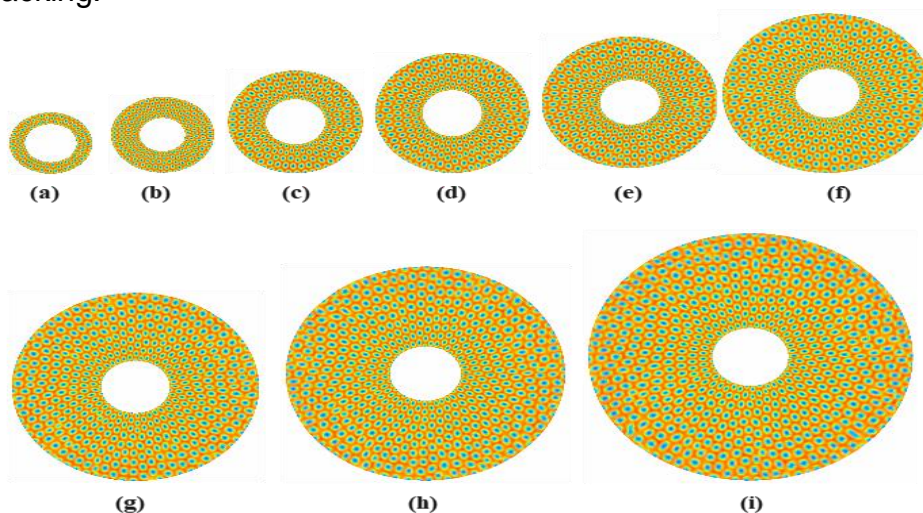
Figure 15: Cylindrical forming system in circular annular discs with neutral walls at $r_a = 3$ in pore size d = 2 in (a), d = 3 in (b), d = 4 in (c), d = 5 in (d), d = 6 in (e), d = 7 in (f), d = 8 in (g), d = 9 in (h) and d = 10 in (i)

This demonstrates that as the system's pore size increases, spiral arms grow broader and cylinders align on spiral rays in the pore geometry. The experimental work demonstrates that the confinement's frustration disrupts the microdomains' natural hexagonal packing.
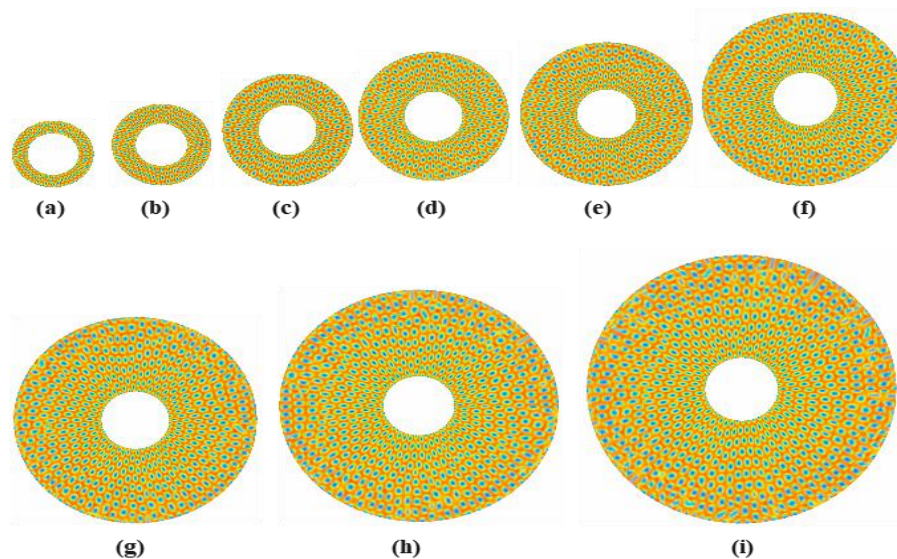
Figure 16: Cylindrical forming system in circular annular discs with neutral walls at $r_a = 5$ in pore size d = 2 in (a), d = 3 in (b), d = 4 in (c), d = 5 in (d), d = 6 in (e), d = 7 in (f), d = 8 in (g), d = 9 in (h) and d = 10 in (i)

Figure 16 shows the simulation of cylindrical morphologies in an annular circular disk with neutral walls. Now $r_a = 5$ and the outer radius is determined by pore size (2, 3, 4, 5, 6, 7, 8, 9 and 10), which is 7, 8, 9, 10, 11, 12, 13, are 14 and 15.

The annular circular disc simulation results for a cylindrical shape with neutral walls are shown in Figure 17. The internal radius is fixed $r_a = 7$ and the pore sizes d are 2, 3, 4, 5, 6, 7, 8, 9 and 10. The outer radii are 9, 10, 11, 12, 13, 14, 15, 16 and 17 respectively. In addition, the pore system's exterior radius expands at different values and the pore system's inner radius rises at two fixed values, $r_a = 5$ and $r_b = 7$. In the pore geometry of both pore systems, similar patterns of the cylindrical forming system are observed. It has been discovered that the cylindrical forming systems were packed with spiral lines in the pore geometry as a result of the curvature effect. Hexagonal packing of microdomains is also observed within the pore structure.
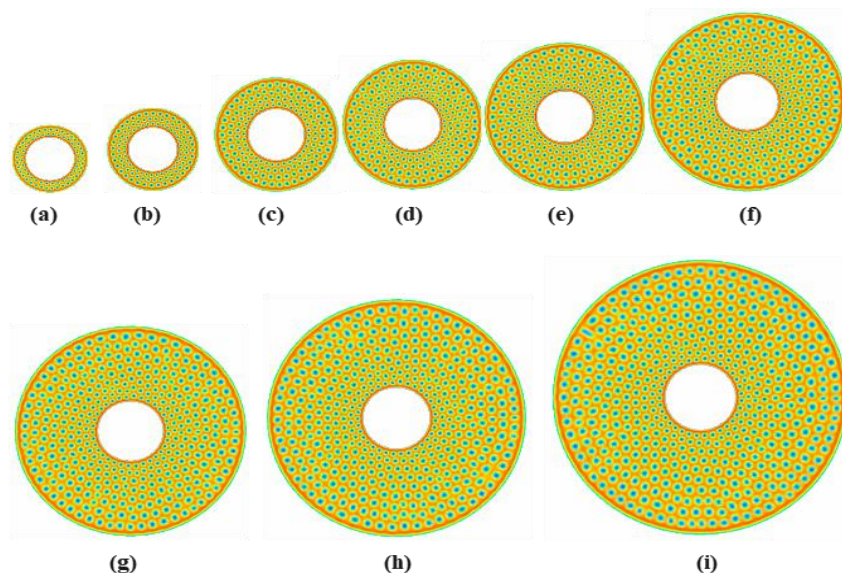

Figure 17: Cylindrical forming system in circular annular discs with neutral walls at $r_a = 7$ in pore size d = 2 in (a), d = 3 in (b), d = 4 in (c), d = 5 in (d), d = 6 in (e), d = 7 in (f), d = 8 in (g), d = 9 in (h) and d = 10 in (i)

3.5 Cylindrical forming simulation with attractive walls

The system being studied is a diblock copolymer that naturally forms cylindrical structures in melt. It is confined inside a circular annulus pore (ring-shaped pore with an inner and outer circular wall). One of the circular walls is preferentially attracted to one block of the D-block copolymer.

The reason for this is the difference in the volume fraction of the blocks and the interaction strength. The reason for this is the difference in the volume fraction of the blocks and the interaction strength. This means one wall is more compatible with one block than the other. The strength of this preferential attraction is $\alpha = 0.2$. α is a measure of how strongly one wall interacts with the preferential block. The confinement and preferential attraction are in the radial r direction only.

This means the pore constrains the system between two circular walls, and one wall attracts specifically to one block, both effects being along the radius of the annulus only. The parameter $d = r_b - r_a$ is pore size.

Fix internal radii $r_a = 3, 5$ or 7 and tune external radii r_b for various pore sizes. For the first set of results, the simulation also includes a wall attracting specifically to one of the monomer types, acting only along the radial direction within the annular pore space. The morphological behaviour of diblock copolymers in a one-dimensional circular annular confinement using our CDS simulations is investigated.

The findings show that microdomains are oriented by surface preference to align in concentric circular rings around the centre of the pore. However, some microdomains are packing along asymmetric spiral lines inside the pore shape. Packing dissatisfaction, which results from the interaction of curvature and confinement factors warping the usual spiral structure. In simple terms, the simulation with one surface attracting to monomer A causes the small domains inside to stack up in concentric rings rather than spiral shapes.

Figure 18: Cylindrical forming system in circular annular discs with attractive walls at $r_a = 3$ in pore size d = 2 in (a), d = 3 in (b), d = 4 in (c), d = 5 in (d), d = 6 in (e), d = 7 in (f), d = 8 in (g), d = 9 in (h) and d = 10 in (i)

The simulation results of an annular circular disc for cylindrical morphology with attractive walls ($\alpha = 0.2$) are shown in Figure 18. The pore sizes d are tuned at 2, 3, 4, 5, 6, 7, 8, 9 and 10. The internal radius $r_a = 3$ and the outer radii are ranged from 5 to 13. At pore size $d = 2$, cylinders are arranged in two rings of concentric circles. At pore size $d = 3$, system contained 3 concentric circles of microdomains.

Cylinders are arranged in 4 concentric rings in the pore system of dimension d = 4. We observe an increase in the number of cylindrical domain rings in the pore system as pore size d increases. Ten rings of cylinders with a pore size of 10 are present.
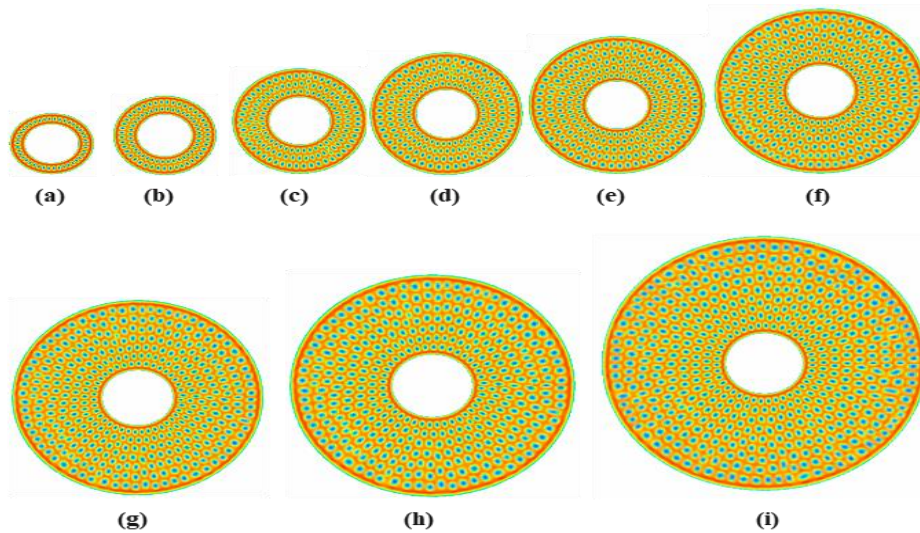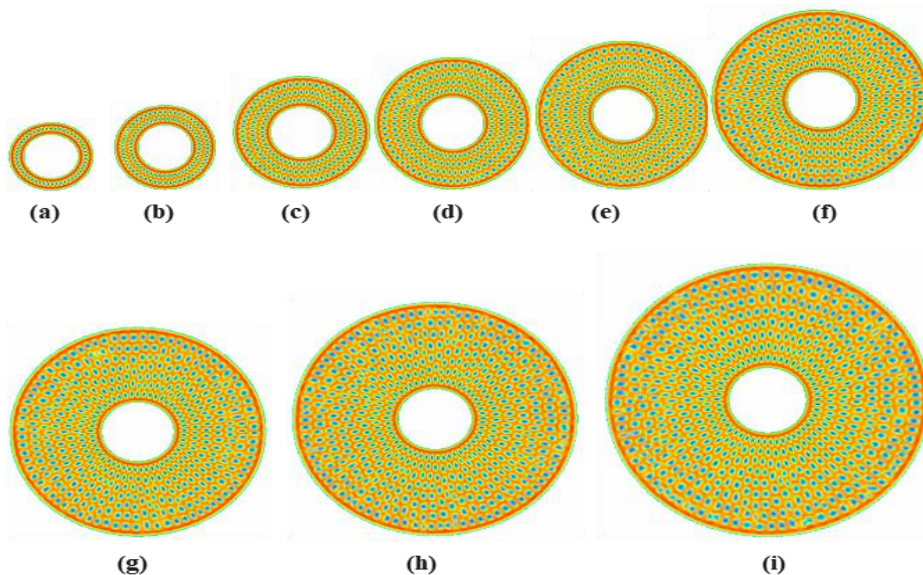
Figure 19: Cylindrical forming system in circular annular discs with attractive walls at $r_a = 5$ in pore size d $= 2$ in (a), d $= 3$ in (b), d $= 4$ in (c), d $= 5$ in (d), d $= 6$ in (e), d $= 7$ in (f), d $= 8$ in (g), d $= 9$ in (h) and d $= 10$ in (i)

The simulation results of an annular circular disc for cylindrical morphology with attractive walls ($\alpha = 0.2$) are shown in Figure 19. The pore size d is tuned from 2 to 10, the internal radius $r_a = 3$ and the outer radii are 7, 8, 9, 10, 11, 12, 13, 14 and 15.

Figure 20: Cylindrical forming system in circular annular discs with attractive walls at $r_a = 7$ in pore size d $= 2$ in (a), d $= 3$ in (b), d $= 4$ in (c), d $= 5$ in (d), d $= 6$ in (e), d $= 7$ in (f), d $= 8$ in (g), d $= 9$ in (h) and d $= 10$ in (i)

The simulation results of an annular circular disc for cylindrical morphology with attractive walls ($\alpha = 0.2$) are shown in Figure 20. The pore sizes d is set at 2, 3, 4, 5, 6, 7, 8, 9 and

10, the internal radius is fixed at $r_a = 3$ and the outer radii are tuned from 9 to 17. We use our CDS simulations to investigate the morphological behavior of diblock copolymers in a one-dimensional circular annular confinement. The findings show that microdomains are oriented by surface preference to align in concentric circular rings around the center of the pore. However, some microdomains are packed along asymmetric spiral lines inside the pore shape. Packing dissatisfaction results from the interaction of curvature and confinement factors warping the usual spiral structure.

3.6 Spherical forming simulation with neutral walls

Circular annular pores of various sizes replicate a spherical forming block copolymer. Analysis of the self-assembling structure is done both with and without attractive walls between the blocks. Figure 21 depicts the cell dynamic simulation for the spherical forming system with a grid size of $30 \times 60 \times 1$. Internal radius is fixed at $r_a = 3$ and interaction strength $\alpha = 0$. External radius $r_b = 6$, and pore size $d = 3$.
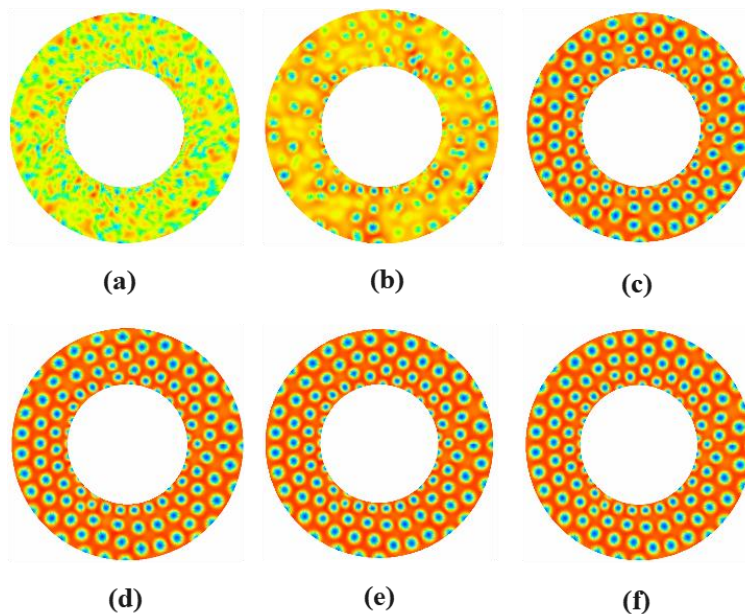

Figure 21: Spherical forming system at various time steps, including t=10 in (a), t=100 in (b), t=1000 in (c), t=10000 in (d), t=100000 in (e), and t=1000000 in (f)

To improve the parameters for reproducing experimental characteristic domain sizes, the model constants are also being adjusted. Under confinement in a circular annular pore of different sizes, an AB diblock copolymer system that naturally forms spheres is being investigated.

Table 5: Spherical morphologies in polar discs with neutral walls at $r_a = 3$

A	B	D	u	v	f	τ	r_a	α
1.50	0.01	0.50	0.58	2.30	0.40	0.20	3	0

The spherical forming system in annular discs of various pore sizes without attractive walls are studied. The interior radius is fixed at 3 and different pore sizes of the annular disc are achieved by tuning the exterior radius of the annular disc.

The annular pore system's order parameters (ψ) were initialized in the range of $-0.5 \leq \psi \leq 0.5$ to produce the simulation results for the sphere-forming system. The order parameter ψ control the χN (degree of segregation between the two blocks). The CDS parameters for the simulation of the sphere system, which included a greater temperature entry than in earlier simulations, are shown in Table 5.
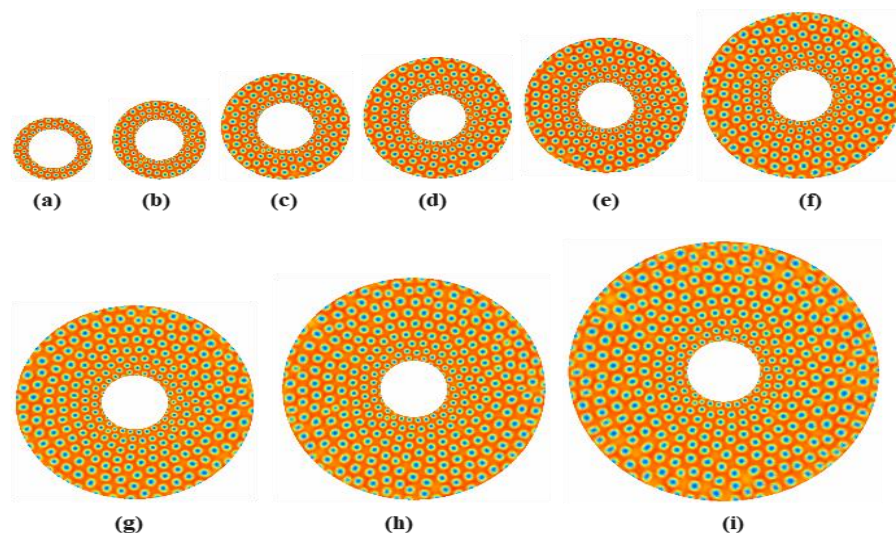

Figure 22: Spherical forming system in circular annular discs with neutral walls at $r_a = 3$ in pore size $d = 2$ in (a), $d = 3$ in (b), $d = 4$ in (c), $d = 5$ in (d), $d = 6$ in (e), $d = 7$ in (f), $d = 8$ in (g), $d = 9$ in (h) and $d = 10$ in (i)

The simulation results of an annular circular disc for spherical morphology with neutral walls are shown in Figure 22. The variable pore sizes d are from 2, 3, 4, 5, 6, 7, 8,9 to 10, the fixed internal radius $r_a = 3$ and the outer radii are 5, 6, 7, 8, 9, 10, 11, 12 and 13 respectively.

A hexagonal configuration of the sphere-forming system is observed in the pore geometry. The presence of spherical nanostructures is obvious in the pore system. In Figure 22, it is demonstrated that the sphere-forming system is arranged in spiral lines and a hexagonal matrix. The spiral linings of spheres are likely to disappear with the increase in pore size, but hexagonal packing of spheres persists.
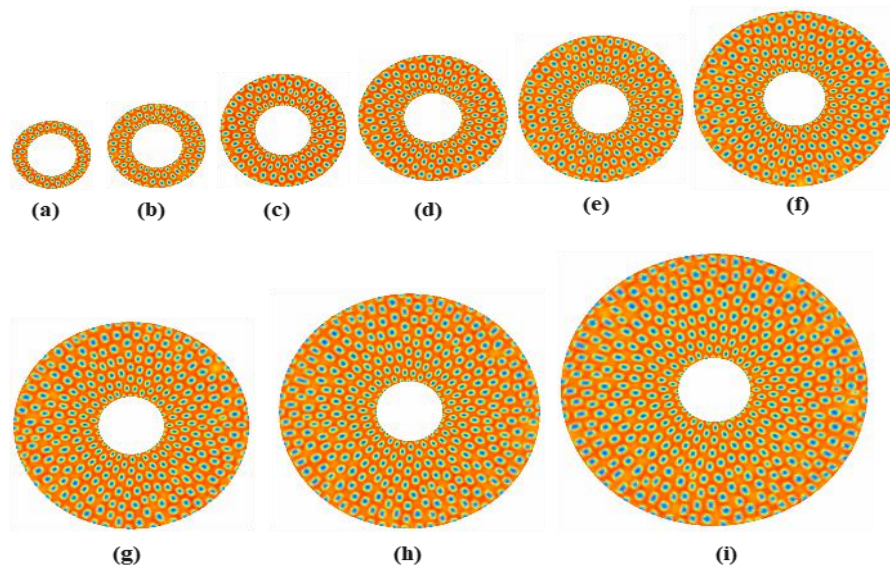
Figure 23: Spherical forming system in circular annular discs with neutral walls at $r_a = 5$ in pore size d = 2 in (a), d = 3 in (b), d = 4 in (c), d = 5 in (d), d = 6 in (e), d = 7 in (f), d = 8 in (g), d = 9 in (h) and d = 10 in (i)

The simulation results of an annular circular disc for spherical morphology with neutral walls are shown in Figure 3.18. The pore size d is set at 2, 3, 4, 5, 6, 7, 8, 9 and 10, interior radius is fixed at $r_a = 5$ and the outer radii of the discs are varied from 7, 8, 9, 10, 11, 12, 13, 14 to 15.
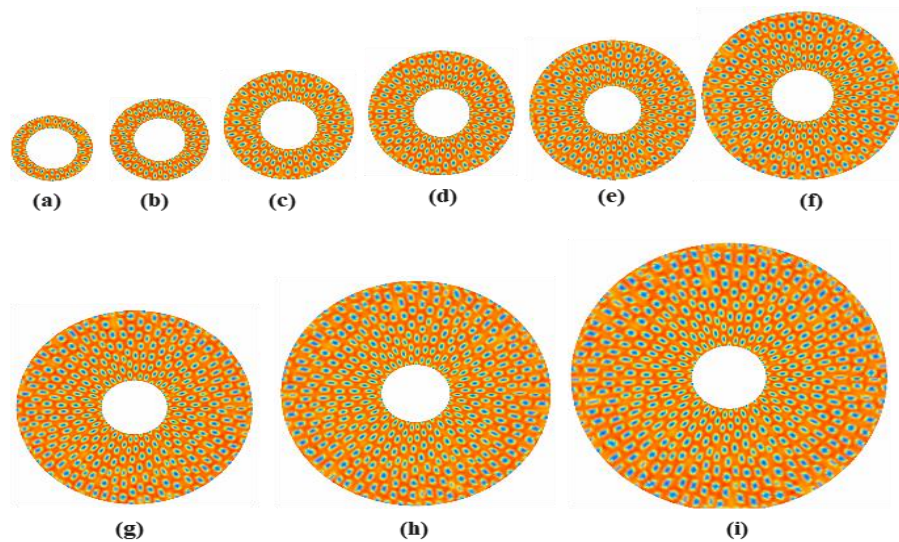

Figure 24: Spherical forming system in circular annular discs with attractive walls at $r_a = 7$ in pore size d = 2 in (a), d = 3 in (b), d = 4 in (c), d = 5 in (d), d = 6 in (e), d = 7 in (f), d = 8 in (g), d = 9 in (h) and d = 10 in (i)

The simulation results of an annular circular disc for spherical morphology with neutral walls are shown in Figure 24. The pores size d are tuned as 2, 3, 4, 5, 6, 7, 8, 9, 10 the internal radius is fixed at $r_a = 7$ and the outer radius is 9, 10, 11, 12, 13, 14, 15, 16, and 17. In pore-sized systems with internal radii 5 and 7 respectively, the spherical arrangements reflect distorted spiral alignments due to the curvature effect as well as larger internal radii in pores.

3.7 Spherical forming simulation with attractive walls

The simulation results of an annular circular disc for spherical morphology with attractive walls ($\alpha = 0.2$) are shown in Figure 3.13. The variable d, pore size is set at 2, 3, 4, 5, 6, 7, 8, 9 and 10, the internal radius $r_a = 3$ while outer radii are tuned from 5, 6, 7, 8, 9, 10, 11, 12 to 13.
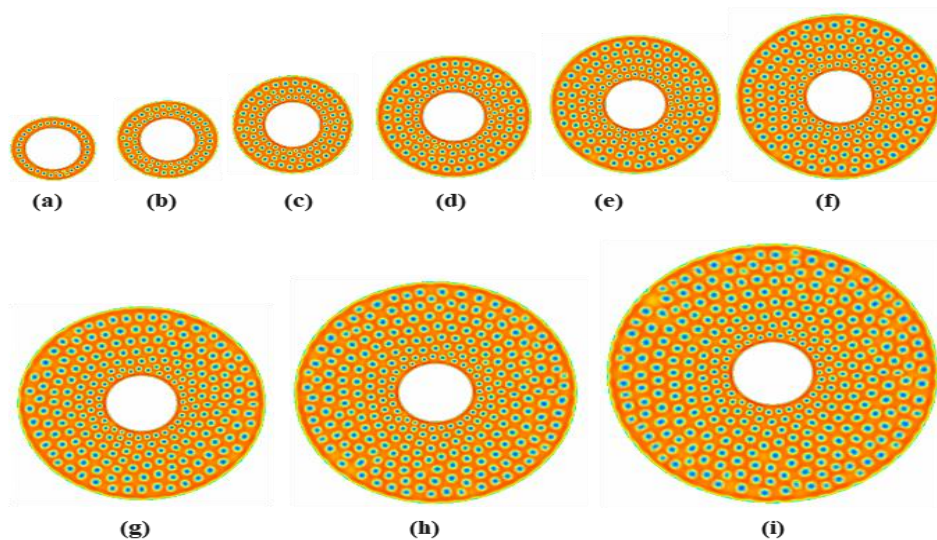

Figure 25: Spherical forming system in circular annular discs with attractive walls at $r_a = 3$ in pore size d $= 2$ in (a), d $= 3$ in (b), d $= 4$ in (c), d $= 5$ in (d), d $= 6$ in (e), d $= 7$ in (f), d $= 8$ in (g), d $= 9$ in (h) and d $= 10$ in (i)

The simulation results have been achieved for the sphere-forming system confined in the annular disc. One-dimensional confinement by attaching one of the polymer segments to the circular walls' affinity is applied. The inner and exterior circular walls of the pore system are used as boundary conditions for one-dimensional confinement, with a specified interaction strength.

A reduction in the temporal parameter in Table 5 is to achieve the sphere-forming system with the help of the CDS model. Simulation results demonstrate the B block of the diblock copolymers system in annular disc conforms into concentric circles in the pore geometry, correspondingly to pore diameters.
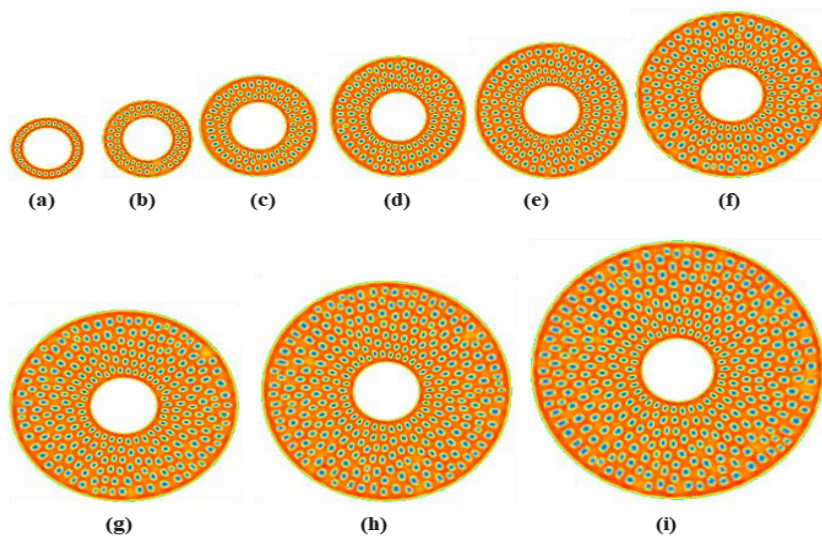
Figure 26: Spherical forming system in circular annular discs with attractive walls at $r_a = 5$ in pore size d = 2 in (a), d = 3 in (b), d = 4 in (c), d = 5 in (d), d = 6 in (e), d = 7 in (f), d = 8 in (g), d = 9 in (h) and d = 10 in (i)

The simulation results of an annular circular disc for spherical morphology with attractive walls ($\alpha = 0.2$) are shown in Figure 26. The pore size d is set at 2, 3, 4, 5, 6, 7, 8, 9 and 10, the internal radius of pore is fixed at $r_a = 5$ and the outer radii are 7, 8, 9, 10, 11, 12, 13, 14 and 15. Some hexagonal microdomains are achieved. A lack of spiral concentration is observed due to increasing internal radius and pore sizes as well.
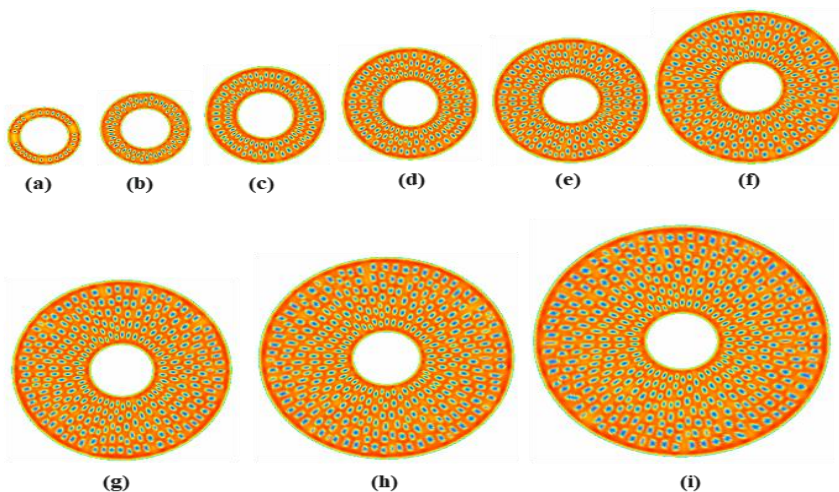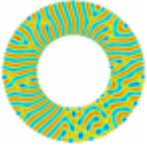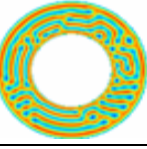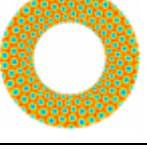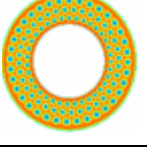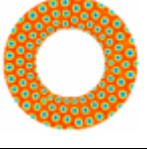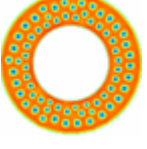

Figure 27: Spherical forming system in circular annular discs with attractive walls at $r_a = 7$ in pore size d= 2 in (a), d = 3 in (b), d = 4 in (c), d = 5 in (d), d = 6 in (e), d = 7 in (f), d = 8 in (g), d = 9 in (h) and d = 10 in (i)

The simulation results of an annular circular disc for spherical morphology with attractive walls ($\alpha = 0.2$) are shown in Figure 27. In this simulation configuration, the pore sizes vary from 2 to 10. The internal radius is set at $r_a = 7$. The outer radii are 9, 10, 11, 12,

13, 14, 15, 16, and 17. The morphology of a diblock copolymer in a circular-annular pore geometry is investigated using the CDS model. A strong interaction occurs between the A monomer and the confined circular walls of the pore. Simulation results generated in this small region reveal the organization of microdomains into concentric spherical rings. Still, some microdomains are distorted into a rhombohedral pattern by confinement, a deviation from the normal concentric alignment.

4. COMPARISON WITH OTHER STUDIES

Predicted results	Comparison with other studies	
	[75] Block copolymers: synthesis, self-assembly and applications	[76] Cell dynamic simulations of diblock copolymer/colloid Systems
	[77] Directing the self-assembly of block copolymers	[78] Self-assembly of diblock copolymers under confinement
	[75] Block copolymers: synthesis, self-assembly, and applications	[76] Cell dynamic simulations of diblock copolymer/colloid Systems
	[79] Hybrid time-dependent Ginzburg–Landau simulations of block copolymer nanocomposites. Reproduced from	[80] Block copolymer-directed assembly of nanoparticles.
	[81] Square patterns formed from the directed self-assembly of block copolymers	[82] Self-assembly in ultrahigh molecular weight sphere-forming diblock copolymer thin films under strong confinement.
	[75] Block copolymers: synthesis, self-assembly, and applications	[81] Square patterns formed from the directed self-assembly of block copolymers

5. CONCLUSION

Using CDS, we simulated diblock copolymers that form lamellae, cylinders, and spheres under circular annular confinement for different pore sizes, both with and without appealing walls. An asymmetric lamella-former oriented perpendicular to the outer wall and preferred parallel to the inner wall is part of the neutral wall system. This preference

for orientation shows how the circular pore shape affects how block copolymer microdomains self-assemble. The CDS simulations showed that several perforated and junction lamellar morphologies, including y, u, w, v and ta curved circular annular pore geometry produces shapes. Fingerprint textures with neutral walls produced perforated lamella with holes centered, isolated, or clustered. Concentric parabolic lamellar alignment is created by attractive walls close to external borders, changing to parallel strips at greater sizes directed perpendicular to the outer circular wall. The pore geometry carefully directs block copolymer assembly. Our CDS simulations demonstrated that lamellae develop parallel strips directed at circular boundaries in larger interior radius pores. Consistent with the experiment, pore geometry, and confinement cause concentric circular lamellar organization resembling a dartboard, especially when appealing circular walls are present. The findings show that microdomains coalesce into concentric lamellae within the pore under curvature and wall influences.

Additionally, innovative cylindrical morphologies formed in irregular spiral patterns are made possible by neutral annular pores. The cylindrical spiral packing changes into a conventional hexagonal arrangement in big pores. Microdomains under interacting circular wall confinement exhibit concentrated circular ring packing. Analogous patterns are formed by spherical morphologies along spirals and parabolas with boundary openings. Additionally, this work presented novel CDS parameters that allow for the simulation of morphologies unique to circular confinement that have not been studied before. Smaller system sizes result in circles with spiral curves, whereas large circular pore systems yield circles with conventional hexagonal packing patterns, according to the results obtained using the CDS parameters.

The size and form of the spherical system with adjusted CDS parameters are decreasing in the presence of interfacial circular barriers. The spherical system displays a packing pattern in concentric circular rings under the geometrical confinement of annular circular pores with interfacial circular walls. The findings demonstrate that the microdomains create packing arrangements in concentric circular rings when curvature is present. In contrast, the nanodomains display a spiral packing pattern when there is curvature and interfacial circular walls.

Reference

1) Feynman, R. P. (1959). "There's Plenty of Room at the Bottom," in APS Annual Meetings, California, December 29, 1959, 22–36.

2) Taniguchi, N. (1974). "On the Basic Concept of Nano-Technology," in Proc. Int. Cong. Prod. Eng., Tokyo, August 26–29, 1974, 18–23.

3) Bayda, S., Adeel, M., Tuccinardi, T., Cordani, M., & Rizzolio, F. (2019). The history of nanoscience and nanotechnology: from chemical–physical applications to nanomedicine. *Molecules*, 25(1), 112.

4) Singh, A., Dubey, S., & Dubey, H. K. (2019). Nanotechnology: The future engineering. *Nanotechnology*, *6*(2), 230-3.

5) Doi, M. (2013). *Soft matter physics.* oxford university press.

6) Banerjee, Arindam, and Ian W. Hamley. "Introduction to peptide soft materials." *Soft Matter* 16.44 (2020): 9998-10000.

7) Hamley, I. W. (2005). Nanoshells and nanotubes from block copolymers. *Soft Matter*, 1(1), 36-43.

8) Chung, S.-W., Ginger, D. S., Morales, M. W., Zhang, Z., Chandrasekhar, V., Ratner, M. A., et al. (2005). Top-Down Meets Bottom-Up: Dip-Pen Nanolithography and DNA-Directed Assembly of Nanoscale Electrical Circuits. Small 1, 64–69.

9) Hobbs, R. G., Petkov, N., and Holmes, J. D. (2012). Semiconductor Nanowire Fabrication by Bottom-Up and Top-Down Paradigms. *Chem. Mater.* 24, 1975–1991.

10) Mullen, E., and Morris, M. A. (2021). Green Nanofabrication Opportunities in the Semiconductor Industry: A Life Cycle Perspective. *Nanomaterials* 11, 1085.

11) Hu, X.-H., and Xiong, S.-S. (2021). Advanced Lithography: Directed Self-Assembly. Chin. J. Appl. Chem. 38, 1029–1078.

12) Yoo, H. G., Byun, M., Jeong, C. K., and Lee, K. J. (2015). Performance Enhancement of Electronic and Energy Devices via Block Copolymer Self-Assembly.

13) Griffiths, R. A., Williams, A., Oakland, C., Roberts, J., Vijayaraghavan, A., and Thomson, T. (2013). Directed Self-Assembly of Block Copolymers for Use in Bit Patterned Media Fabrication. J. Phys. D: Appl. Phys. 46, 503001.

14) Alvarez-Fernandez, A., Fleury, G., Ponsinet, V., Walmsness, P. M., and Kildemo, M. (2020). Formation and Optical Response of Self-Assembled Gold Nanoparticle Lattices on Oxidized Silicon Synthesized Using Block Copolymers. J. Vac. Sci. Technol. B 38, 013601.

15) Sadegh, F., Akin, S., Moghadam, M., Keshavarzi, R., Mirkhani, V., Ruiz-Preciado, M. A., et al. (2021). Copolymer-Templated Nickel Oxide for High-Efficiency Mesoscopic Perovskite Solar Cells in Inverted Architecture. Adv. *Funct. Mater*. 31, 2102237.

16) Kang, H. S., Han, S. W., Park, C., Lee, S. W., Eoh, H., Baek, J., ... & Park, C. (2020). 3D touchless multiorder reflection structural color sensing display. *Science Advances*, 6(30), eabb5769.

17) Guo, L., Wang, Y., & Steinhart, M. (2021). Porous block copolymer separation membranes for 21st century sanitation and hygiene. *Chemical Society Reviews*, 50(11), 6333-6348.

18) Black, C. T., Ruiz, R., Breyta, G., Cheng, J. Y., Colburn, M. E., Guarini, K. W., et al. (2007). Polymer Self Assembly in Semiconductor Microelectronics.

19) Doerk, G. S., Li, R., Fukuto, M., and Yager, K. G. (2020). Wet Brush Homopolymers as "Smart Solvents" for Rapid, Large Period Block Copolymer Thin Film Self-Assembly. *Macromolecules* 53 (3), 1098–1113.

20) P. Chen, X. He and H. Liang, "Effect of surface field on the morphology of a symmetric diblock copolymer under cylindrical confinement," J. *Chem. Phys*., vol. 124, pp. 104906-1-104906-6, 2006.

21) P. Chen and H. Liang, "Origin of microstructures from confined asymmetric diblock copolymers," *Macromolecules*, vol. 40, pp. 7329-7335, 2007.

22) M. Yiyong and E. Adi, "Self-assembly of diblock copolymers," *Chem Soc Rev*, vol. 41, pp. 5969-5985, 2012.

23) Case, L. J., Bates, F. S., & Dorfman, K. D. (2023). Tuning conformational asymmetry in particle-forming diblock copolymer alloys. *Soft Matter*, 19(1), 90-97.

24) Xie, J., & Shi, A. C. (2023). Phase Behavior of Binary Blends of Diblock Copolymers: Progress and Opportunities. *Langmuir*, 39(33), 11491-11509.

25) Gavrilov, A. A., Shupanov, R. M., & Chertovich, A. V. (2020). Phase Diagram for Ideal Diblock-Copolymer Micelles Compared to Polymerization-Induced Self Assembly. *Polymers,* 12(11), 2599.

26) Xie, J., Lai, C. T., & Shi, A. C. (2023). Regulating the self-assembly of AB/CD diblock copolymer blends via secondary interactions. *Journal of Polymer Science*.

27) Stevens, M. P. (1990). Polymer chemistry (Vol. 2). New York: Oxford university press.

28) Zhao, F., Xu, Z., & Li, W. (2021). Self-Assembly of Asymmetric Diblock Copolymers under the Spherical Confinement. *Macromolecules*, *54*(24), 11351-11359.

29) Karayianni, M., & Pispas, S. (2021). Block copolymer solution self-assembly: Recent advances, emerging trends, and applications. *Journal of Polymer Science*, 59(17), 1874-1898.

30) Chi, P., Wang, Z., Li, B., & Shi, A. C. (2011). Soft confinement-induced morphologies of diblock copolymers. *Langmuir*, 27(18), 11683-11689.

31) Sanz, A., Nogales, A., & Ezquerra, T. A. (2011). From hard to soft confinement in a symmetric block copolymer: local and segmental dynamics. *Soft Matter*, 7(14), 6477-6483.

32) Diaz, J., Pinna, M., Breen, C., Zvelindovsky, A., & Pagonabarraga, I. (2023). Block Copolymer Nanocomposites under Confinement: Effect on Frustrated Phases. *Macromolecules*, 56(13), 5010-5021.

33) M. Pinna and A. V. Zvelindovsky, "Large scale simulation of block copolymers with cell dynamics," Eur. Phys. J. B, vol. 85, pp. 210, JUN, 2012.

34) J. Feng and E. Ruckenstein, "Morphologies of AB diblock copolymer melt confined in nano cylindrical tubes," *Macromolecules*, vol. 39, pp. 4899-4906, 2006.

35) b. Yu, P. Sun, T. Chen, Q. Jin, D. Ding, B. Li and A. Shi, "Confinement-induced novel morphologies of block copolymers," PRL, vol. 96, pp. 138306-1-138306-4, 2006.

36) Yang, G. G., Choi, H. J., Han, K. H., Kim, J. H., Lee, C. W., Jung, E. I., ... & Kim, S. O. (2022). Block copolymer nanopatterning for nonsemiconductor device applications. ACS *Applied Materials & Interfaces*, 14(10), 12011-12037.

37) Xiang, H., Shin, K., Kim, T., Moon, S., McCarthy, T. J., & Russell, T. P. (2005). The influence of confinement and curvature on the morphology of block copolymers. Journal of Polymer Science Part B: *Polymer Physics*, 43(23), 3377-3383.

38) Wu, Y., Cheng, G., Katsov, K., Sides, S. W., Wang, J., Tang, J., ... & Stucky, G. D. (2004). Composite mesostructures by nano-confinement. *Nature materials*, 3(11), 816-822.

39) Yang, J., Dong, Q., Liu, M., & Li, W. (2022). Universality and specificity in the self-assembly of cylinder-forming block copolymers under cylindrical confinement. *Macromolecules*, 55(6), 2171-2181.

40) Inayatullah Soomro, I. A., Shah, S. B., Majid, A., Muhammad, R., Hameed, A., Abas, G., ... & Ahmed, W. (2019). Mathematical Modelling of Cylindrical Forming Di-block Co-polymers confined in circular annular pores. IJCSNS, 19(2), 16.

41) Vasil, G. M., Burns, K. J., Lecoanet, D., Olver, S., Brown, B. P., & Oishi, J. S. (2016). Tensor calculus in polar coordinates using Jacobi polynomials. *Journal of Computational Physics*, 325, 53-73.

42) Daly, P. (1974). Polar geometry waveguides by finite-element methods. IEEE Transactions on Microwave Theory and Techniques, 22(3), 202-209.

43) Cabré, X. (2008). Elliptic PDE's in probability and geometry: symmetry and regularity of solutions. Discrete and Continuous Dynamical Systems, 20(3), 425.

44) Lam, C. Y. (1994). Applied numerical methods for partial differential equations: an introduction with spreadsheet programs. Prentice-Hall.

45) Iqbal, M. J., Soomro, I., Bibi, M., & Mallah, R. N. (2023). Morphological investigation of lamellae patterns in diblock copolymers under change of thickness and confinement in polar geometry. VFAST Transactions on Mathematics, 11(2), 174-197.

46) Iqbal, M. J., Soomro, I., & Mahar, M. H. (2024). Re-patterning of cylindrical packing of diblock copolymers under confinement and curvature effects by using approximations of PDE's involved in the CDS model on polar mesh system. Journal of Physics Communications, 8(8), 085001.

47) Iqbal, M. J., Soomro, I., & Gulzar, U. (2024). Patterns of nanoporous spherical packing emerging under influence of curvature and confinement. VFAST Transactions on Mathematics, 12(1), 121-136.

48) https://www.lgjdxcn.asia/public_article.php?article=394

49) Iqbal, M. J., Soomro, I., Mahar, M. H., & Gulzar, U. (2024). Exploring Long-Range Order in Diblock Copolymers through Cell Dynamic Simulations. VFAST Transactions on Software Engineering, 12(2), 31-45.

50) Wu, H. T., & Zhang, Y. M. (2016). A second-order finite difference method for the two-dimensional Laplace equation in polar coordinates. *Journal of Computational Physics*, 313, 305-319.

51) Zhang, G. H., & Cheng, Y. M. (2012). A fourth-order compact finite difference scheme for the two-dimensional Laplace equation in polar coordinates. *Journal of Computational Physics*, 231(1), 79-95.

52) Shih, Y. T., & Chen, C. S. (2009). Finite difference method for solving the two-dimensional Laplace equation in polar coordinates with nonuniform grid spacing. *Journal of Computational Physics*, 228(9), 3228-3244.

53) Zhou, H., & Yin, X. (2017). Numerical solution of the two-dimensional Laplace equation in polar coordinates by a non-uniform finite difference scheme. *Journal of Applied Mathematics and Computing,* 54(1-2), 229-245.

54) Leveque, R. (1998). Finite difference methods for differential equations.

55) LeVeque, R. J. (2007). Finite difference methods for ordinary and partial differential equations: steady-state and time-dependent problems. *Society for Industrial and Applied Mathematics*.

56) Dhumal, M. L., & Kiwne, S. B. (2014). Finite difference method for Laplace equation. *International Journal of Statistics and Mathematics*, 9, 11-13.

57) Xu, Y., Xie, N., Li, W., Qiu, F., & Shi, A. C. (2012). Phase behaviors and ordering dynamics of diblock copolymer self-assembly directed by lateral hexagonal confinement. *The Journal of Chemical Physics*, 137(19).

58) Qi, S., & Wang, Z. G. (1997). Kinetics of phase transitions in weakly segregated block copolymers: Pseudostable and transient states. *Physical Review*, 55(2), 1682.

59) Luo, K., & Yang, Y. (2002). Lamellar orientation and corresponding rheological properties of symmetric diblock copolymers under steady shear flow. *Macromolecules,* 35(9), 3722-3730.

60) Luo, K., & Yang, Y. (2002). Lamellar orientation and corresponding rheological properties of symmetric diblock copolymers under steady shear flow. *Macromolecules,* 35(9), 3722-3730.

61) Ghasimakbari, T., & Morse, D. C. (2020). Order-disorder transitions and free energies in asymmetric diblock copolymers. *Macromolecules*, 53(17), 7399-7409.

62) Seo, Y., Brown, J. R., & Hall, L. M. (2015). Effect of tapering on morphology and interfacial behavior of diblock copolymers from molecular dynamics simulations. *Macromolecules*, 48(14), 4974-4982.

63) Matsen, M. W. (2003). New fast SCFT algorithm applied to binary diblock copolymer/homopolymer blends. *Macromolecules*, 36(25), 9647-9657.

64) Zhao, B., Dong, Q., Yang, W., & Xu, Y. (2023). Theoretical Study of Phase Behaviors of Symmetric Linear B1A1B2A2B3 Pentablock Copolymer. *Molecules*, 28(8), 3536.

65) Hamley, I. W. (2000). Cell dynamics simulations of block copolymers. *Macromolecular theory and simulations*, 9(7), 363-380.

66) Oono, Y., & Puri, S. (1987). Computationally efficient modeling of ordering of quenched phases. *Physical review letters*, 58(8), 836.

67) Oono, Y., & Puri, S. (1988). Study of phase-separation dynamics by use of cell dynamical systems. I. Modeling. *Physical Review A*, 38(1), 434.

68) Puri, S., & Oono, Y. (1988). Study of phase-separation dynamics by use of cell dynamical systems. II. Two-dimensional demonstrations. *Physical Review A*, 38(3), 1542.

69) Pinna, M., & Zvelindovsky, A. V. (2012). Large scale simulation of block copolymers with cell dynamics. *The European Physical Journal B*, 85, 1-18.

70) Ohta, T., & Kawasaki, K. (1986). Equilibrium morphology of block copolymer melts. *Macromolecules*, 19(10), 2621-2632.

71) Kawasaki, K., Ohta, T., & Kohrogui, M. (1988). Equilibrium morphology of block copolymer melts. 2. *Macromolecules*, 21(10), 2972-2980.

72) Hamley, I. W. (2000). Cell dynamics simulations of block copolymers. *Macromolecular theory and simulations*, 9(7), 363-380.

73) Diaz, J., Pinna, M., Zvelindovsky, A. V., & Pagonabarraga, I. (2022). Nematic Ordering of Anisotropic Nanoparticles in Block Copolymers. *Advanced Theory and Simulations*, 5(1), 2100433.

74) Diaz, J., Pinna, M., Zvelindovsky, A. V., Asta, A., & Pagonabarraga, I. (2017). Cell dynamic simulations of diblock copolymer/colloid systems. *Macromolecular Theory and Simulations*, 26(1), 1600050.

75) Feng, H., Lu, X., Wang, W., Kang, N. G., & Mays, J. W. (2017). Block copolymers: Synthesis, self-assembly, and applications. *Polymers*, 9(10), 494.

76) Diaz, J., Pinna, M., Zvelindovsky, A. V., Asta, A., & Pagonabarraga, I. (2017). Cell dynamic simulations of diblock copolymer/colloid systems. *Macromolecular Theory and Simulations*, 26(1), 1600050.

77) Darling, S. B. (2007). Directing the self-assembly of block copolymers. *Progress in polymer science*, 32(10), 1152-1204.

78) Shi, A. C., & Li, B. (2013). Self-assembly of diblock copolymers under confinement. *Soft Matter*, 9(5), 1398-1413.

79) Diaz, J., Pinna, M., Zvelindovsky, A. V., & Pagonabarraga, I. (2022). Hybrid Time-Dependent Ginzburg–Landau Simulations of Block Copolymer Nanocomposites: Nanoparticle Anisotropy. *Polymers*, 14(9), 1910.

80) Thompson, R. B., Ginzburg, V. V., Matsen, M. W., & Balazs, A. C. (2002). Block copolymer-directed assembly of nanoparticles: Forming mesoscopically ordered hybrid materials. *Macromolecules*, 35(3), 1060-1071.

81) Li, W., & Gu, X. (2021). Square patterns formed from the directed self-assembly of block copolymers. *Molecular Systems Design & Engineering*, 6(5), 355-367.

82) Cao, W., Xia, S., Appold, M., Saxena, N., Bießmann, L., Grott, S., ... & Müller-Buschbaum, P. (2019). Self-Assembly in ultrahigh molecular weight sphere-forming diblock copolymer thin films under strong confinement. *Scientific reports*, 9(1), 18269.